Biogeochemical controls on carbonate dynamics driven by methane and freshwater inputs in shallow sediments of a brackish continental shelf sea

Katarzyna Łukawska-Matuszewska[1], Grzegorz Rzepa[2], Aleksandra Brodecka-Goluch[1], Andrzej Borkowski[2], Beata Gebus-Czupyt[3], Artur Błachowski[2], Maciej Manecki[2], Jarosław Kania[2], Maciej Dwornik[2], Magdalena Radzikowska[3]

[1]Faculty of Oceanography and Geography, University of Gdańsk, al. Marszałka J. Piłsudskiego 46, 81-378 Gdynia, Poland
[2]Faculty of Geology Geophysics and Environmental Protection, AGH University of Krakow, al. Mickiewicza 30, 30-059 Kraków, Poland
[3]Institute of Geological Sciences Polish Academy of Sciences, Twarda Str. 51/55, 00-818 Warsaw, Poland

Correspondence to: Katarzyna Łukawska-Matuszewska (katarzyna.lukawska-matuszewska@ug.edu.pl)

Abstract. Continental shelf seas are essential to the carbon cycle, supporting nearly one-third of global marine primary production and significantly contributing to the burial of organic and inorganic carbon. Processes such as organoclastic sulfate reduction (OSR), methane production or anaerobic oxidation of methane (AOM), occurring in coastal sediments, have a significant impact on the carbon cycling in the marine environment. That impact may be modified by an increased organic matter (OM) supply or freshwater input. In the present interdisciplinary study, we investigated carbonate dynamics in three benthic environments of a brackish continental shelf sea: (1) anoxic sediments dominated by OSR; (2) nearshore sediments with high terrigenous OM input and active methanogenesis; and (3) sediments influenced by groundwater infiltration and pore-water freshening, coupled with methanogenesis. We analyzed pore-water chemistry (DIC, total alkalinity, major ions, nutrients), sediment geochemistry (CH_4, total organic carbon, total nitrogen, total sulfur), and mineralogy, including authigenic carbonates and iron sulfides. We used stable isotopes of DIC (δ^{13}C-DIC), methane (δ^{13}C-CH_4, δ^{2}H-CH_4) and organic matter (δ^{13}C, δ^{15}N) to trace carbon transformations. We also determined rates of OSR and AOM experimentally. Based on these data, we have proposed conceptual models of carbon cycling in the three sedimentary environments. In the methane-free sediment, organic matter degradation was primarily governed by OSR, producing 54 mmol m^{-2} d^{-1} of DIC within the top 100 cm, accompanied by limited carbonate burial and dominant pyrite accumulation. In sediments where the flux of OM exceeded sulfate supply, a substantial portion of OM remineralization shifted to methanogenesis in the uppermost decimeters, leading to rapid sulfate depletion, a shoaled sulfate–methane transition, and elevated DIC concentrations; these processes were especially pronounced in sediments affected by freshwater seepage, where pore water freshening further limited sulfate availability. In such conditions carbonate dynamics were markedly enhanced: methane-related processes - in particular AOM, which reached up to 1077 μmol dm^{-3} d^{-1} in freshwater-influenced sediments - produced additional DIC, contributed to carbonate supersaturation and promoted pronounced authigenic carbonate (mainly dolomite) formation. Depth-integrated DIC production from AOM (331 mmol m^{-2} d^{-1} over 0–100 cm)

substantially exceeded OSR-derived DIC (58 mmol m^{-2} d^{-1}) in these settings, corresponding with elevated authigenic dolomite burial rates (467–994 μmol m^{-2} d^{-1}). To our knowledge, this study provides the first quantitative estimate of authigenic carbonate burial rates for Baltic Sea sediments.

1 Introduction

Continental shelf seas cover ~7% of the global ocean surface but play a disproportionate role in the carbon (C) cycle. They support 10–30% of global marine primary production due to high nutrient availability (Bauer et al., 2013). Shelf sediments account for 30–50% of marine inorganic C burial and ~80% of organic C burial (Bauer et al., 2013; Liu et al., 2010).

Over recent decades, enhanced nitrogen and phosphorus inputs from watersheds have intensified coastal eutrophication (Rabalais et al., 2010; Paerl et al., 2014). In shallow systems, a large fraction of organic matter (OM) from primary production reaches the seabed (Berner, 1982; Hedges and Keil, 1995; Wollast, 1998; Cai, 2011; Bauer et al., 2013). The oxidation of OM in surface sediments follows a redox cascade determined by available electron acceptors (Froelich et al., 1979). Under oxic conditions aerobic respiration dominates. Degradation of the increased OM resulting from eutrophication rapidly consumes oxygen and promotes the expansion of bottom water hypoxia and anoxia (Rabalais et al., 2010; Fennel and Testa, 2019). Once bottom-water O_2 is depleted, OM oxidation shifts to anaerobic pathways via denitrification, reduction of Mn(IV), Fe(III) and sulfate (SO_4^{2-}), although their relative importance depends on local electron-acceptor availability and sedimentary conditions.

Organoclastic sulfate reduction (OSR) commonly dominates in coastal and margin sediments accounting for up to 70% of OM oxidation (Thamdrup and Canfield, 1996; Jørgensen and Kasten, 2006). When OM supply exceeds SO_4^{2-} availability, methanogenesis occurs (Froelich et al., 1979). Most biogenic methane (CH_4) produced in subsurface environment is oxidized within sediments, predominantly by sulfate-driven anaerobic oxidation of methane (SO_4^{2-}–AOM) at the sulfate–methane transition (SMT) zone, where downward-diffusing sulfate meets upward-migrating methane (Boetius et al., 2000; Beulig et al., 2019; Egger et al., 2018); however CH_4 may also be oxidized anaerobically with nitrate (In't Zandt et al., 2018), Mn(IV), or Fe(III) (Beal et al., 2009; Sturm et al., 2019).

Degradation of OM in marine sediment contributes to the production of dissolved inorganic carbon (DIC) (Table S1: R1-R6). Anaerobic reactions (Table S1: R2-R5) additionally lead to the production of total alkalinity (TA). Methanogenesis itself does not change TA (Table S1: R6); anaerobic CH_4 oxidation, however, increases both DIC and TA (Table S1: R12–R14). Overall, anoxic diagenesis elevates DIC and TA in pore waters relative to seawater (e.g. Chatterjee et al., 2011). Sediments therefore act as internal alkalinity sources to the water column (Chen, 2002; Thomas et al., 2009). This flux may buffer seawater against acidification driven by rising atmospheric pCO_2 (Friedlingstein et al., 2020). Elevated alkalinity also promotes supersaturation with respect to carbonate minerals and favors authigenic carbonate precipitation (Baker and Burns, 1985; Jørgensen, 1992). In this way, sediments may constitute a long-term sink for inorganic C (Akam et al., 2020).

Porewater alkalinity can be also modified by reoxidation of reduced by-products of OM degradation. Reoxidation consumes alkalinity (Table S1: R7–R11) and lowers pH, promoting $CaCO_3$ dissolution (Table S1: R17). By contrast, precipitation and preservation of reduced species as authigenic minerals - for example the reaction of sulfide with Fe(III) to form pyrite (Table S1: R15) - yields a net alkalinity gain and favors carbonate precipitation (Mucci et al., 2000; Budrige, 2011). This process is also considered as a long-term sink for both iron and sulfur, because pyrite is thermodynamically stable (Chanton et al., 1987).

Sedimentary processes described above have important implications for the carbon cycle and are particularly important in shallow shelf seas with strong benthic-pelagic coupling (Rassmann et al., 2016; Griffiths et al., 2017). The Baltic Sea represents such a system. It is a shallow, semi-enclosed water body with substantial riverine input and pronounced eutrophication. High sedimentation rates and elevated OM supply enhance rates of anaerobic remineralization, producing high concentrations of DIC in subsurface sediments. Relatively low sulfate availability from reduced salinity together with high input of OM promote shallow methanogenesis (Egger et al., 2018) and causes the SMT to shift upward toward the sediment surface (Jilbert et al., 2021). Local fresh groundwater discharge may also influence the progression of these processes by further lowering sulfate availability. In shallow Baltic waters, release of DIC and TA from anoxic sediments can significantly modify water-column chemistry (Gustafsson et al., 2019). Alternatively, precipitation of authigenic carbonates can act as a long-term sedimentary sink for inorganic carbon, which is especially relevant in the Baltic Sea where planktonic calcifiers are largely absent except in the westernmost region (Tyrrell et al., 2008).

This study investigates carbonate dynamics in three benthic environments of a continental shelf sea: (1) anoxic sediments dominated by OSR; (2) nearshore sediments with high terrigenous OM input and active methanogenesis; and (3) sediments influenced by groundwater infiltration and pore-water freshening, coupled with methanogenesis.

We aim to constrain the biogeochemical controls on DIC and TA production and on authigenic carbonate precipitation. We analyzed pore-water chemistry (DIC, TA, major ions, nutrients), sediment geochemistry (CH_4, total organic carbon, total nitrogen, total sulfur), and mineralogy (bulk phases and authigenic carbonates and iron sulfides). Stable isotopes of DIC (δ^{13}C-DIC), methane (δ^{13}C-CH_4, δ^{2}H-CH_4), and organic matter (δ^{13}C, δ^{15}N) were used to trace carbon transformations. Rates of OSR and AOM were determined experimentally. Based on these data, we propose conceptual models of carbon cycling in the three sedimentary environments.

2 Materials and methods

2.1 Sampling

Sediment and water samples were collected from three stations located in the Gdańsk Basin (southeastern Baltic Sea) at water depths of 50–103 m: ZGG, MET2, and MET1-MP (Fig. S1). Station MET1-MP represents an active deepwater pockmark influenced by both methane seepage and freshwater infiltration. Station MET2 is characterized by shallow methane accumulation without distinct seabed morphology and freshwater infiltration (Jaśniewicz et al., 2019; Brodecka-

Goluch et al., 2022). Station ZGG, designated as the reference site, shows no evidence of methane occurrence or freshwater discharge. Sampling was conducted from RV *Oceanograf* in July 2023 and February 2024. Hydroacoustic surveys were performed prior to coring using a Reson Teledyne SeaBat 7125 multibeam echosounder, an EdgeTech SB-216S subbottom profiler, and a Simrad EK80 split-beam echosounder to determine precise sampling locations.

Sediment cores were collected with a Rumohr-Lot gravity corer equipped with Plexiglas liners (7.5 cm diameter, 150 cm length). At each station, seven cores (90–110 cm long) were collected during the July 2023 sampling campaign and an additional seven cores in February 2024. These cores were used for analyses of: (1) total organic carbon (TOC), total nitrogen (TN), total sulfur (TS), stable isotopes of organic matter ($\delta^{13}C$, $\delta^{15}N$), loss on ignition (LOI), and water content (W); (2) CH_4, CO_2 and their stable isotopes ($\delta^{13}C$-CH_4, $\delta^{13}C$-CO_2, $\delta^{2}H$-CH_4), and oxidation–reduction potential (ORP); (3) pH and total alkalinity (TA); (4) dissolved inorganic carbon (DIC) and $\delta^{13}C$-DIC; (5) sulfate (SO_4^{2-}), chloride (Cl^-), calcium (Ca^{2+}), magnesium (Mg^{2+}), hydrogen sulfide ($\sum H_2S$, the sum of H_2S, HS^- and S^{2-}), ammonia ($\sum NH_4^+$, the sum of NH_4^+ and NH_3), phosphate (PO_4^{3-}), manganese (Mn^{2+}) and iron (Fe^{2+}) in pore water; (6) mineralogy and micromorphology; and (7) experimental rates of organoclastic sulfate reduction (R_{OSR}) and anaerobic oxidation of methane (R_{AOM}).

Pore waters were extracted from intact, sealed cores using Rhizon® samplers (0.15 µm pore size). For each core liner, 4 mm holes matching the Rhizon® sampler fitting were pre drilled at 5 cm intervals and sealed with a tape. After cores retrieval aboard, the tape was pierced and samplers inserted; to minimize contact with air, cores remained sealed throughout porewater collection. The uppermost sampler (1–4 cm above the sediment surface, depending on station) collected bottom water overlying the core. Porewater was drawn into attached 20 cm^3 plastic syringes. To minimize oxidation, all subsequent subsampling and treatment were performed immediately after porewater sampling. Immediately after extraction, TA, pH, $\sum H_2S$, $\sum NH_4^+$, and PO_4^{3-} were measured onboard. Samples for major ions, Mn^{2+}, and Fe^{2+} were acidified with HNO_3. DIC samples were poisoned with $HgCl_2$ and stored in sealed, nearly full tubes (<1% headspace) at 4°C. Sampling for carbon isotopic composition of DIC ($\delta^{13}C$-DIC) was carried out in an N_2 glove box; porewater samples were collected into 2 cm^3 septum vials that were filled by injecting porewater with one needle while displacing N_2 through a second needle; vials were completely filled with porewater and stored at 4°C prior to analysis.

For CH_4 analysis, sediment was subsampled through 12-mm holes in the liners and transferred immediately to glass vials containing 2.5% NaOH, which were sealed with butyl rubber stoppers and aluminum crimp caps (Jørgensen et al., 2001). NaOH was added to halt microbial activity, preventing biological production or consumption of CH_4. A headspace was equilibrated by shaking, and vials were stored caps-down at 4°C until gas chromatographic analysis. Samples for carbon isotopic composition of methane and carbon dioxide ($\delta^{13}C$-CH_4, $\delta^{13}C$-CO_2) were collected in the same manner as the CH_4 samples but the procedure was carried out inside an N_2 glove box. Instead of adding NaOH, vials were pre filled with Milli Q water.

Cores designated for solid-phase analyses were sectioned at 5 cm intervals using a PVC ring and plastic spatula; samples were taken from the central part of each section. Each sample was placed in a separate polyethylene bag. Samples for microbial analyses were collected from five depth intervals (0–20, 20–40, 40–60, 60–80, and 80–100 cm) using sterile tools.

Samples for mineralogical analyses were taken from 10–15, 40–45, and 80–85 cm. All sediment samples were stored at −21°C until analysis.

2.2 Analytical procedures

2.2.1 Pore-water and bottom-water parameters

Sulfate (SO_4^{2-}) and chloride (Cl^-) concentrations were determined by high-performance ion chromatography (Metrohm 850 Professional IC). Calcium (Ca^{2+}), magnesium (Mg^{2+}), manganese (Mn^{2+}), and iron (Fe^{2+}) were measured using inductively coupled plasma–optical emission spectrometry (ICP-OES; PerkinElmer OPTIMA 8300).

Concentrations of $\sum H_2S$, $\sum NH_4^+$, and PO_4^{3-} were determined spectrophotometrically (Hach-Lange DR6000). The methylene blue method was applied for $\sum H_2S$ (Cline, 1969), the indophenol blue method for $\sum NH_4^+$, and the molybdenum blue method for PO_4^{3-} (Grasshoff et al., 1999). The limit of quantification (LOQ) was 0.03 mmol dm^{-3} for SO_4^{2-} and <2.5 µmol dm^{-3} for other major ions. For Mn^{2+}, Fe^{2+}, $\sum H_2S$, $\sum NH_4^+$, and PO_4^{3-}, LOQ values ranged from 0.05 to 1.00 µmol dm^{-3}. Analytical precision (RSD) was ≤5% for all parameters.

DIC concentrations were measured in duplicate using a VarioTOC Cube analyzer (Elementar GmbH) equipped with a nondispersive infrared detector. Samples were acidified in-line with 1% H_3PO_4, and liberated CO_2 was quantified after purging. Accuracy, based on certified reference material recovery, was 98%. RSD was ≤1%.

Carbon isotopic composition of DIC (δ^{13}C-DIC) was determined using a Thermo Delta V plus isotope ratio mass spectrometer coupled to a Thermo GasBench II under continuous helium flow. Samples were reacted with H_3PO_4 for 24 h at 25°C. The evolved CO_2 was analyzed for carbon isotope composition. Standards NBS-19, NBS-18 were measured with each analytical series. The assigned δ^{13}C values for the standards were: NBS-19 = +1.95‰ and NBS-18 = −5.014‰ (VPDB). Results are reported in δ-notation (‰) relative to Vienna Pee Dee Belemnite (VPDB; Coplen, 2011). Analytical precision was ±0.1‰.

Total alkalinity (TA) was determined by potentiometric titration with 0.01 M HCl using an automatic titrator (SM-Titrino 702, Metrohm). Data were evaluated using the Gran method over pH 4.5–3.5 (10–12 points). pH was monitored with a combined pH/ATC electrode (accuracy ±0.002 units). The HCl titrant was standardized against certified Na_2CO_3 (Sigma-Aldrich) dissolved in 0.2 mol dm^{-3} NaCl to match Baltic Sea ionic strength. Accuracy of TA determination was ≤3 µmol kg^{-1}. Precision was ≤0.2% for standards and ≤0.3% for samples.

pH was measured spectrophotometrically using m-cresol purple as indicator (Hammer et al., 2014). Precision was ≤0.010%. Salinity and dissolved oxygen in bottom water were measured with a WTW Multi 3630 IDS multimeter equipped with TetraCon® 925 and FDO® 925 sensors.

Methane concentrations were determined by the headspace method using a PerkinElmer gas chromatograph equipped with a flame ionization detector and an HP-5 column (30 m × 0.32 mm × 0.25 µm). The detection limit was 0.2 µmol dm^{-3}.

Concentrations were corrected for sediment porosity (φ), calculated from water content (W) after Håkanson and Jansson (1983) and Graca (2006):

$$\varphi = W[(100 - W)d^{-1} + W]^{-1} \quad (1)$$

where W is water content (%) and d is wet bulk density (g cm^{-3}):

$$d = 260(100 + 1.6(W + IG))^{-1} \quad (2)$$

where IG is the loss on ignition (LOI) in percent of wet sediment. LOI was determined after ignition at 450°C to constant mass. Water content was determined by drying at 105°C to constant mass.

Carbon isotopic composition of methane and carbon dioxide ($\delta^{13}C$-CH_4, $\delta^{13}C$-CO_2) was measured using a Finnigan Delta Plus isotope ratio mass spectrometer coupled via a GC Combustion III interface to an HP 6890 gas chromatograph. After chromatographic separation, CH_4 was oxidized at 980°C to CO_2 in a ceramic reactor containing CuO, Cr_2O_3, and Pt catalyst. Calibration employed RM8563, NBS 22, NBS 19, and two certified methane standards (Methane #2 and Methane #7, Indiana University). Results are reported in δ-notation (‰) relative to VPDB (Coplen, 2011). Analytical precision was ±0.2‰. The detection limit for obtaining reliable $\delta^{13}C$ data was 0.1% CH_4. No pre-concentration unit was used.

Hydrogen isotopes in methane ($\delta^{2}H$-CH_4) were determined using a Delta V Plus mass spectrometer coupled via a Conflo IV GC Isolink interface to a Trace GC Ultra chromatograph. Methane was converted to H_2 at 1420°C in a high-temperature reactor. Calibration used VSMOW2, SLAP-2, GISP, and the methane standards Methane #2 and Methane #7. Results are reported relative to Vienna Standard Mean Ocean Water (VSMOW). Analytical precision was ±3‰.

2.2.2 Sediment geochemistry and mineralogy

Total nitrogen (TN), total sulfur (TS), and total organic carbon (TOC) were determined at the Uranium-Series Laboratory, Institute of Geological Sciences, Polish Academy of Sciences (Warsaw, Poland). Wet sediment samples were homogenized and subsamples were weighted, dried overnight at 50°C, and reweighted (Hedges and Stern, 1984). Prior to analysis, carbonates were removed by treating 400 mg of sediment with 20 cm^3 of 1 M HCl for 24 h at 50°C. Samples were rinsed three times with deionized water, dried at 40–50°C, reweighted and ground in an agate mortar. Approximately 5 mg of homogenized material was sealed in tin capsules and combusted at 1150°C using a Vario MicroCUBE elemental analyzer (Elementar). Evolved CO_2, N_2, and SO_2 were separated chromatographically and quantified by thermal conductivity detection. Results were calibrated against sulfanilic acid and reported as wt%. Analytical precision (1σ) was ±0.6% for TOC, ±0.2% for TN, and ±0.4% for TS.

Stable carbon and nitrogen isotopes in organic matter ($\delta^{13}C$, $\delta^{15}N$) were analyzed at the Stable Isotope Laboratory, Institute of Geological Sciences, Polish Academy of Sciences. Measurements were performed using a Flash 1112 HT elemental analyzer coupled via ConFlo IV to a Delta V Advantage isotope ratio mass spectrometer (Thermo Scientific). Samples wrapped in tin foil were combusted at 1020°C. Generated CO_2 and N_2 were purified, chromatographically separated, and introduced into the mass spectrometer. Calibration employed USGS 41a, USGS 40, and IAEA 600 reference materials.

Results are reported in δ-notation (‰) relative to VPDB ($\delta^{13}C$) and atmospheric N_2 ($\delta^{15}N$). Analytical precision (1σ) was ±0.1‰ for $\delta^{13}C$ and ±0.3‰ for $\delta^{15}N$. Each sample was analyzed in duplicate, and mean values are reported.

Mineral composition was characterized by powder X-ray diffraction (PXRD), optical microscopy, scanning electron microscopy with energy-dispersive spectroscopy (SEM-EDS), ^{57}Fe Mössbauer spectroscopy. PXRD data were collected using a Rigaku SmartLab diffractometer with a graphite monochromator and rotating Cu anode. Samples were ground in ethanol in an agate mortar. Mineral composition was quantified by Rietveld full-pattern X-ray diffraction fitting technique using SIROQUANT analysis of randomly oriented powders. Uncertainty of mineral quantification was estimated from the standard deviations of individual scale factors for each phase and is 0.3 wt.% for pyrite, 0.5 wt.% for dolomite, and 0.4 wt.% for calcite. The <2 μm clay fraction was analyzed using oriented mounts prepared as air-dried, ethylene glycol–saturated, and heated (550°C) specimens (Moore and Reynolds, 1997).

SEM analyses of powders and thin sections were performed in low-vacuum mode using a FEI Quanta 200 FEG microscope equipped with an EDS system. Undisturbed, air-dried samples of relevant horizons were embedded in Technovit EPOX resin to prepare thin sections. ^{57}Fe Mössbauer spectroscopy measurements were performed at room temperature applying the RENON MsAa-4 spectrometer (Błachowski et al., 2008) equipped with the LND Kr-filled proportional detector and the $^{57}Co(Rh)$ source. Raman microspectroscopy measurements were performed with a Thermo Scientific DXR Raman Microscope. Spectra were recorded at room temperature using 532 nm diode laser and Olympus (100×) objective lens.

Thermodynamic equilibrium and mineral–water interactions in pore waters were modeled using PHREEQC (version 3.6) with the validated thermodynamic database wateq4f.dat of Parkhurst and Appelo (2013), using the measured pore-water pH (Figure S2) and the measured concentrations of dissolved ions (Figure 2 and 3) as inputs; redox conditions were set from pe values calculated from measured ORP data (Figure S2), and those pe values were subsequently used to calculate dissolved Fe(II) and Fe(III) species.

2.2.3 Dolomite and pyrite burial rates

Dolomite and pyrite burial rates (A; μmol m^{-2} d^{-1}) were calculated as:

$$A = 10^4 \cdot d \cdot [Conc.] \cdot \omega \cdot (100 - W)/100^{-1} \quad (3)$$

where d is wet bulk density of sediment (g cm^{-3}), [Conc.] is mineral concentration (μmol g^{-1} dry weight), ω is linear sedimentation rate (cm d^{-1}), and W is water content (%). Sedimentation rates were 2.06 mm yr^{-1} for MET1-MP, 0.90 mm yr^{-1} for MET2, and 2.01 mm yr^{-1} for ZGG (Zalewska et al., 2020). Burial rates were calculated using mean mineral concentrations for each station. Mineral contents were derived from PXRD data and SEM–EDS elemental distribution maps.

2.2.4 Determination of organoclastic sulfate reduction and anaerobic methane oxidation rates

Rates of organoclastic sulfate reduction (R_{OSR}) and anaerobic oxidation of methane (R_{AOM}) measured in the present study represent potential rates. Incubations were conducted without substrate limitation and thus reflect the maximum metabolic capacity of the microbial community.

For determination of OSR, 10 cm^3 of sediment was mixed with 30 cm^3 of sterile seawater amended with 1% sodium lactate. Lactate was added as an electron donor during sample pre-treatment to ensure that measured H_2S production primarily reflected OSR. From this slurry, 1 cm^3 aliquots (in duplicate) were transferred to incubation cuvettes. Each aliquot was amended with 0.5 cm^3 Na_2SO_4 solution to obtain five substrate concentrations (0–0.1 mol dm^{-3}). Incubations were conducted for 12–14 h at 20°C. For AOM, 2 cm^3 of sediment was placed in sterile 20 cm^3 glass flasks sealed with septum caps. Each flask was injected with 1 cm^3 of ^{13}C-labeled CH_4 (99 atom% ^{13}C; Sigma-Aldrich). Parallel incubations without added substrate were performed to determine basal activity. Incubations lasted 70–76 h at 20°C and were terminated by adding 0.2 cm^3 of tenfold-diluted $HgCl_2$. To analyze sulfate reduction microbial activity, sulfide concentrations were determined spectrophotometrically using N,N-Dimethyl-p-phenyl-enediamine sulfate salt (98%, SigmaAldrich), and the Michaelis–Menten relationship was plotted.

For AOM, produced CO_2 was analyzed using a Delta Plus Finnigan isotope ratio mass spectrometer coupled to a Hewlett Packard 6890 gas chromatograph equipped with a Chrompack packed column (27.5 m × 0.32 mm). Helium (>99.999%) was used as the carrier gas at a constant flow rate of 2 cm^3 min^{-1}. The oven temperature was programmed from 27°C to 60°C at 5°C min^{-1}. Headspace gas (0.1 cm^3) was injected with a split ratio of 1:80. A 0.2% ^{13}C-labeled CO_2 standard was used for calibration.

3 Results

3.1 Distribution of TOC, TN, and TS and stable isotopic composition of carbon ($\delta^{13}C$) and nitrogen ($\delta^{15}N$) in sedimentary organic matter

OM content is highest in surface sediments (0–20 cm) at all stations (Fig. 1). TOC correlates positively with TN (Fig. 1a, b), indicating that nitrogen is predominantly associated with organic matter. TOC ranges from 2.8 to 10.7 wt%, TN from 0.2 to 1.4 wt%, and TS from 0.8 to 3.6 wt% (Fig. 1a–c). The molar TOC:TN ratio varies between 7.4 and 13.7 (Fig. 1d).

The highest OM contents occur at station MET1-MP. TOC ranges from 5.5 to 10.7 wt%, and TN from 0.6 to 1.4 wt%. This station also shows the strongest downcore variability. The lowest OM contents are observed at MET2, with similar values in both seasons. TOC ranges from 2.5 to 5.0 wt% and TN from 0.2 to 0.5 wt%. Station ZGG exhibits intermediate values. TOC ranges from 3.0 to 6.3 wt% and TN from 0.3 to 0.8 wt%.

TS contents exceed 1 wt% at most depths (Fig. 1c). The highest average TS (2.2 wt%) occurs at ZGG. Maximum values (≥3.2 wt%) are recorded at 70–75 cm in both seasons. The lowest average TS (1.2 wt%) occurs at MET2. At MET1-MP, mean TS is 1.7 wt%. The TOC:TN ratio at MET1-MP ranges from 7.4 to 9.1. At ZGG, values range from 8.7 to 11.9. The highest ratios occur at MET2 (9.3–13.7).

Sediment oxidation–reduction potential (ORP) ranges from −502 to −5 mV. The highest values occur in surface layers (Fig. S2). Loss on ignition (LOI) ranges from 5.5 to 20.2 wt% (Fig. S2). Values are highest at MET1-MP (13.5–20.2 wt%), intermediate at ZGG (6.5–14.4 wt%), and lowest at MET2 (5.5–10.5 wt%). Water content (W) follows a similar pattern (Fig.

S2). The highest values occur at MET1-MP (67.4–97.7%). At ZGG, W ranges from 66.0 to 90.6%. At MET2, W ranges from 50.4 to 79.5%.

The isotopic composition of organic carbon ($\delta^{13}C$) ranges from −27.3 to −24.4‰, and that of nitrogen ($\delta^{15}N$) from 1.2 to 6.7‰ (Fig. 1e, f). The lowest $\delta^{13}C$ values occur at station ZGG in both seasons. The highest values are observed at MET2 in summer. The largest $\delta^{13}C$ variability (~1.5‰) is recorded at ZGG (−27.3 to −25.5‰) and MET2 (−26.0 to −24.4‰). At MET1-MP, $\delta^{13}C$ varies within a narrower range (<1‰), from −26.2 to −25.2‰. The greatest $\delta^{15}N$ variability occurs at MET2 (1.2–6.7‰). At this station, deeper sediments are depleted in ^{15}N relative to surface layers. The depletion reaches ~3‰ in the deepest intervals. At MET1-MP and ZGG, $\delta^{15}N$ varies over a narrower range (2.0–4.5‰).

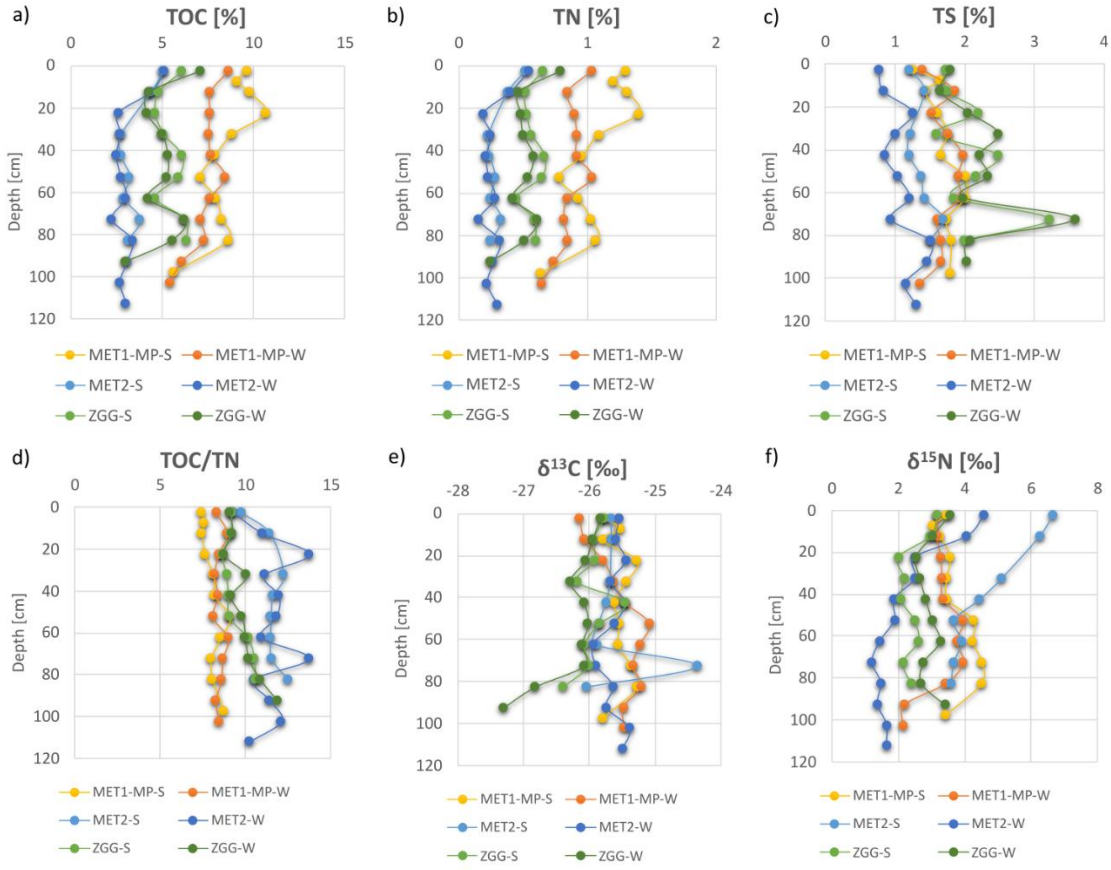

Figure 1: Depth distribution of total organic carbon (TOC), total nitrogen (TN), and total sulfur (TS), molar TOC:TN ratio, and stable isotopic composition of carbon ($\delta^{13}C$) and nitrogen ($\delta^{15}N$) in sedimentary organic matter at the reference station (ZGG), the methane-influenced station (MET2), and the station affected by both methane and freshwater discharge (MET1-MP). Data are shown for summer 2023 (S) and winter 2024 (W).

3.2 Composition of pore water and bottom water

Results from summer and winter show that spatial differences among stations exceed seasonal variability (Figs. 2, 3). Depth profiles of major ions (Cl^-, SO_4^{2-}, Ca^{2+}, Mg^{2+}) are shown in Fig. 2. The concentration of Cl^- ranges from 70.30 mmol dm^{-3} to 180.40 mmol dm^{-3}, SO_4^{2-} from 0.03 mmol dm^{-3} to 9.23 mmol dm^{-3}, Ca^{2+} from 2.52 mmol dm^{-3} to 4.84 mmol dm^{-3}, while Mg^{2+} from 8.34 mmol dm^{-3} to 18.37 mmol dm^{-3}.

Major-ion concentrations in bottom water and surface-most sediments reflect salinity. Salinity is highest at ZGG (12.2 in summer; 12.1 in winter) and lowest at MET2 (8.0 in summer; 7.5 in winter). At MET2, Cl^-, Ca^{2+}, and Mg^{2+} remain nearly constant with depth. In contrast, these ions decrease markedly with depth at MET1-MP. At ZGG, Ca^{2+} increases significantly downcore. Sulfate remains relatively high (≥3.5 mmol dm^{-3}) throughout the ZGG profile. At MET1-MP and MET2, sulfate is restricted to the upper 30–40 cm.

$\sum H_2S$ reaches maximum concentrations at ZGG (up to 2026 µmol dm^{-3}). At MET1-MP and MET2, $\sum H_2S$ ranges from <LOQ to 1783 µmol dm^{-3} and is confined to discrete sediment intervals (Fig. 2e), corresponding to zones of sulfate-dependent methane oxidation. Bottom waters at MET2 are oxic (3.1 mg dm^{-3} O_2 in summer; 5.9 mg dm^{-3} in winter). At ZGG and MET1-MP, O_2 concentrations are <0.2 mg dm^{-3} in summer and <1.7 mg dm^{-3} in winter.

Pore-water Fe^{2+} concentrations are generally <30 µmol dm^{-3} (Fig. 2h). Elevated values occur only at MET1-MP, reaching 139.3 µmol dm^{-3} below 60 cm in summer. Mn^{2+} concentrations range from <LOQ to 51.6 µmol dm^{-3}, with highest values at ZGG (Fig. 2g).

$\sum NH_4^+$ ranges from 22.2 to 3794.9 µmol dm^{-3}. PO_4^{3-} ranges from 1.4 to 950.2 µmol dm^{-3}. Both species attain maximum concentrations at MET1-MP (Fig. 3d, e). At ZGG and MET2, concentrations are lower, ranging from 22.2 to 2027.0 µmol dm^{-3} for $\sum NH_4^+$ and from 1.4 to 361.1 µmol dm^{-3} for PO_4^{3-}.

The pH at all sampling sites was from 7.00 to 8.31, with an average of 7.57±0.21 at station MET1-MP, 7.66±0.26 at station MET2, and 7.57±0.20 at station ZGG (Fig. S2).

The TA in the pore water varied in the range of 1911.3-32747.2 µmol kg^{-1}. Overall, the highest TA in pore waters was found in the sediment of pockmark MET1-MP, while the lowest values were observed at ZGG, similarly to DIC, which is the main component of TA in seawater (Fig. 3a).

DIC concentrations range from 1851 to 33,323 µmol kg^{-1} (Fig. 3b). The highest values occur at MET1-MP. The lowest concentrations and the smallest downcore variability are observed at the non-methane station ZGG.

The $\delta^{13}C$-DIC values range from −16.2‰ to 17.3‰ (Fig. 3c). At ZGG, $\delta^{13}C$-DIC remains negative throughout the profile. At MET2, negative values are restricted to the upper ~25 cm, whereas deeper layers show positive values. At MET1-MP, $\delta^{13}C$-DIC exhibits limited variability. Negative values occur only in the surface layer (0–5 cm) during summer.

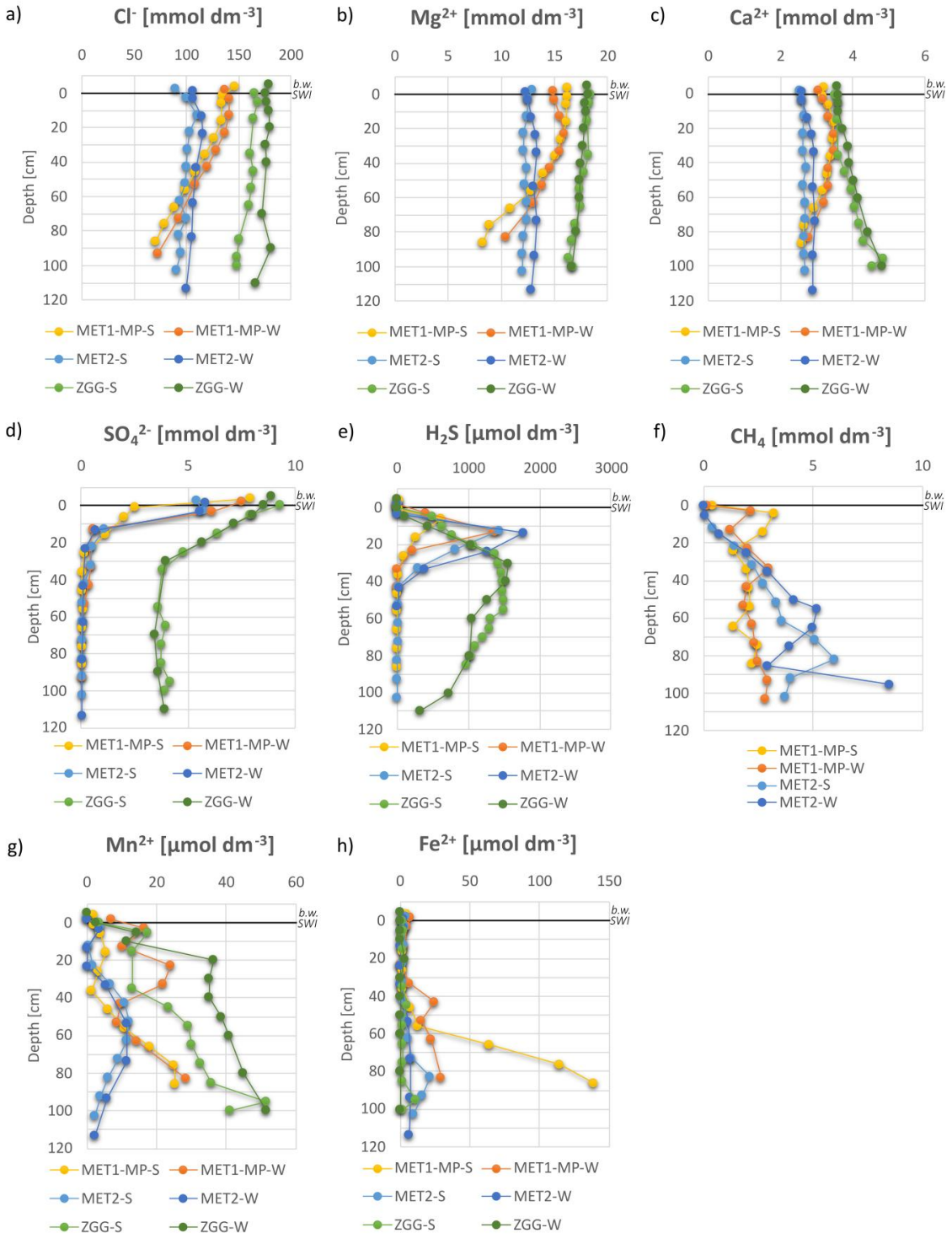

303

304 **Figure 2: Concentrations of (a) chloride, (b) magnesium, (c) calcium, (d) sulfate, (e) hydrogen sulfide, (f) methane, (g) manganese,**
305 **and (h) iron in bottom water (b.w.) and pore water at the reference station (ZGG), the methane-influenced station (MET2), and**

the station affected by both methane and freshwater discharge (MET1-MP) during summer 2023 (S) and winter 2024 (W). SWI denotes the sediment–water interface.

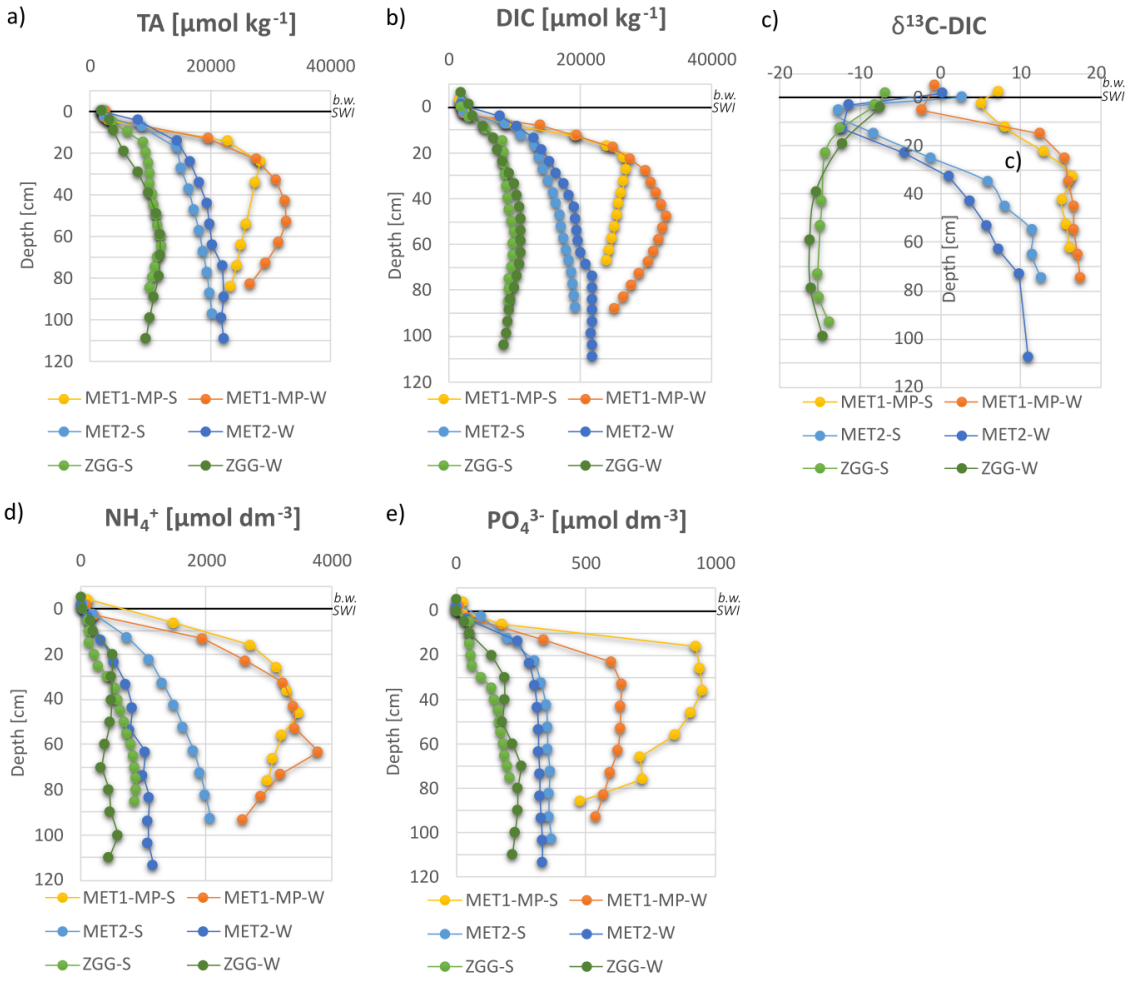

Figure 3: Total alkalinity (TA) (a), dissolved inorganic carbon (DIC) (b), stable carbon isotopic composition of DIC (δ^{13}C-DIC) (c), ammonium (d), and phosphate (e) concentrations in bottom water (b.w.) and pore waters. Labels as in Fig. 2.

3.3 Methane concentration and stable C and H isotopes in gases

Methane concentrations at MET1-MP range from 0.17 to 3.24 mmol dm^{-3}, and at MET2 from <LOQ to 8.49 mmol dm^{-3} (Fig. 2f). At MET1-MP, maximum CH_4 concentrations occur near the sediment surface (~5 cm bsf). Concentrations decrease with depth and stabilize at ~2 mmol dm^{-3}. At MET2, CH_4 increases progressively with depth and reaches a maximum at ≤80 cm bsf. Methane is not detected at ZGG.

Depth profiles of $\delta^{13}C\text{-}CH_4$, $\delta^{2}H\text{-}CH_4$, and $\delta^{13}C\text{-}CO_2$ at MET1-MP and MET2 are shown in Fig. S3. At MET1-MP, $\delta^{13}C\text{-}CH_4$ ranges from −62.6 to −55.8‰. At MET2, values are lower, from −76.6 to −69.6‰. The $\delta^{2}H\text{-}CH_4$ values range from −271 to −257‰ at MET1-MP and from −250 to −239‰ at MET2. At MET2, $\delta^{13}C\text{-}CO_2$ remains negative throughout the profile (−8.1 to −2.6‰). At MET1-MP, $\delta^{13}C\text{-}CO_2$ ranges from −1.0 to 5.7‰ and is predominantly positive, except in the surface layer and at ~90 cm bsf.

3.4 Rate of organoclastic sulfate reduction and anaerobic methane oxidation

The measured rates of organoclastic sulfate reduction (R_{OSR}) and anaerobic oxidation of methane (R_{AOM}) presented in Table 1 represent the maximum metabolic capacity of the microbial community (potential rates); incubations were conducted without substrate limitation and therefore reflect relative microbial activity between samples rather than absolute in situ rates.

R_{OSR} ranges from 15 to 164 µmol dm^{-3} d^{-1} (Table 1). At ZGG, values range from 24 to 46 µmol dm^{-3} d^{-1}. At MET2, rates vary between 21 and 48 µmol dm^{-3} d^{-1}. The highest variability occurs at MET1-MP (16–163 µmol dm^{-3} d^{-1}). At MET1-MP and MET2, maximum rates are observed in the 0–20 cm interval. At ZGG, the highest R_{OSR} occurs at 20–40 cm depth.

R_{AOM} ranges from 6 to 1077 µmol dm^{-3} d^{-1}. At MET1-MP, rates are elevated throughout the profile (59–1077 µmol dm^{-3} d^{-1}). Maximum values occur at 40–60 cm and 80–100 cm depth (Table 1). At MET2, R_{AOM} is lower (6–33 µmol dm^{-3} d^{-1}) and is concentrated in surface sediments. At ZGG, rates are relatively uniform with depth (8–10 µmol dm^{-3} d^{-1}). Additional raw data concerning the determination of OSR and AOM are provided in the Supplementary Materials (Tables S2 and S3).

Table 1: Organoclastic sulfate reduction (R_{OSR}) and anaerobic methane oxidation (R_{AOM}) rates (mean of two replicates), and the corresponding DIC production calculated from the stoichiometry of OSR (R1) and AOM (R3), at the reference station (ZGG), the methane-influenced station (MET2), and the station affected by both methane and freshwater discharge (MET1-MP).

Station	Sediment layer	R_{OSR}	R_{AOM}	Depth integrated rates			
				R_{OSR}	$R_{DIC\text{-}OSR}$	R_{AOM}	$R_{DIC\text{-}AOM}$
	[cm]	[µmol dm^{-3} d^{-1}]		[mmol m^{-2} d^{-1}]			
MET1-MP	0-20	164	95				
	20-40	23	106				
	40-60	15	1077	29	58	331	331
	60-80	16	59				
	80-100	18	731				
MET2	0-20	21	33				
	20-40	48	6				
	40-60	36	7	29	59	9	9
	60-80	31	9				
	80-100	42	8				
ZGG	0-20	24	10				
	20-40	46	9	27	54	7	7
	40-60	25	10				
	60-80	34	9				

	80-100	33	8

Depth-integrated R_{OSR} and R_{AOM} (0–100 cm) and the corresponding DIC production are summarized in Table 1. DIC production from OSR is comparable among stations. In contrast, MET1-MP exhibits exceptionally high R_{AOM} and associated DIC production, exceeding values at the other stations by two orders of magnitude. The lowest process rates and DIC production occur at ZGG.

3.5 Mineralogy

The studied sediments are fine-grained (Brodecka et al., 2013) and classified as silt (MET1-MP), sandy silt (MET2), and clayey silt (ZGG). They are dominated by a matrix composed of clay minerals, biogenic silica, and organic matter (Fig. S5). This matrix constitutes ~20–50 vol% of the sediment and generally increases with depth. At MET1-MP it ranges from 30 to 54%, at MET2 from 20 to 39%, and at ZGG from 36 to 53%.

Detrital aluminosilicates (mainly quartz, feldspars, and micas) occur as dispersed grains within this matrix. Their proportion remains relatively constant at MET2 (~30–35%) but decreases with depth at MET1-MP (13 to 8%) and ZGG (24 to 13%).

PXRD analyses of bulk samples (Fig. S6) and clay fractions (Fig. S7) indicate that phyllosilicates are dominated by mica/illite, chlorite, and kaolinite. A ~17 Å reflection in glycolated samples that disappears upon heating indicates mixed-layer illite–smectite. The position of the (*060*) reflection is consistent with dioctahedral phyllosilicates (Moore and Reynolds, 1997). Microscopy also reveals glauconite, an Fe-rich mica-group mineral. It occurs sporadically at MET1-MP and MET2 and is more common at ZGG.

Authigenic carbonates and sulfides are minor components (< several wt%; Table 2). Pyrite (FeS_2) is the dominant sulfide. It occurs as isolated euhedral crystals (cubic or octahedral, ≤1 µm) or as framboids with diameters of a few to ~20 µm (Fig. 4). Irregular framboidal aggregates also occur. Pyrite framboids are commonly associated with diatom frustules or organic-rich domains. Microscopy and PXRD indicate higher average pyrite contents at ZGG than at MET1-MP and MET2 (Table 2).

Table 2: Dolomite and pyrite contents in sediments (range and mean values determined by PXRD and SEM–EDS elemental mapping) and corresponding burial rates. Burial rates are reported as mean values (based on PXRD and SEM–EDS) and as ranges derived from both methods within a 0-85 cm sediment column.

Station	Dolomite (PXRD)	Dolomite (SEM)	Pyrite (PXRD)	Pyrite (SEM)	Dolomite burial rate	Pyrite burial rate
	wt%				µmol m^{-2} d^{-1}	
MET1-MP	2.9-4.9 (**3.9**)	3.9-12.2 (**7.2**)	3.7-7.2 (**5.9**)	1.8-11.6 (**6.8**)	XRD: 484±13 SEM: 888±87 (467-994)	XRD: 556±18 SEM: 640±153 (453-828)
MET2	0.0-2.9 (**2.0**)	0.1-8.1 (**4.0**)	2.3-5.6 (**3.5**)	2.5-18.9 (**8.0**)	XRD: 254±58 SEM: 517±7 (184-525)	XRD: 341±5 SEM: 785±4 (334-789)
ZGG	0.0-1.4	0.0-4.6	5.4-9.4	2.3-21.7	XRD: 60±35	XRD: 959±16

	(**0.4**)	(**0.8**)	(**7.4**)	(**10.5**)	SEM: 136±110 (1-271)	SEM: 1341±87 (940-1447)

Dolomite [$CaMg(CO_3)_2$] is the predominant carbonate phase. Its presence is indicated by the 2.88 Å reflection in PXRD patterns (Fig. S6). Due to low concentrations, unambiguous interpretation is not possible because diffraction peaks (*101*), (*015*) and (*021*) indicative of space group of dolomite (Gregg et al., 2015; Lukoczki et al., 2026) are not apparent. However, SEM–EDS analyses (Fig. S8) show near-equimolar Ca and Mg, consistent with dolomite rather than high-Mg calcite. Also Raman microspectroscopy of carbonate crystals revealed typical dolomite (and not Mg-calcite) features (Fig. S9): strong sharp bands at 1100 cm^{-1} (symmetric stretching), 305 cm^{-1} (librational mode), and 180 cm^{-1} (translational mode), as well as weak bands at 730 cm^{-1} and 1445 cm^{-1}, related to in-plane bending and asymmetric stretching, respectively (Sun et al., 2014, Zheng et al., 2021, Alves et al., 2023). Comparison of the Raman spectra with that of proper dolomite (Rędziny quarry, Southern Poland, Kowalski et al., 1976) indicates that the band broadening (Sun et al., 2014, Zheng et al., 2021) that should be associated with structural disorder (expected in protodolomite and high-Mg calcite) does not occur, as the band half-widths are of the same order as for crystalline dolomite (Fig. S9b). Moreover, euhedral to subhedral rhombohedral habits are typical for authigenic dolomite (Fig. 4), and not nanocrystalline aggregates characteristic of protodolomite (Liu et al., 2020, Zheng et al., 2021). Therefore, despite the lack of unambiguous PXRD evidence, both the chemical composition, morphology, and Raman features suggest that the dominant carbonate in the sediments is dolomite.

Dolomite is most abundant at MET1-MP, slightly less abundant at MET2, and nearly absent at ZGG (Table 2). At MET1-MP, dolomite forms euhedral crystals several to ~20 μm in size (Fig. 4). At MET2, both fine (<20 μm) euhedral or subhedral crystals and larger subhedral to anhedral grains occur. The euhedral/subhedral morphology of many of the crystals indicates that they are authigenic. At ZGG, small (5–10 μm) subhedral to anhedral grains are restricted to the subsurface layer (10–15 cm).

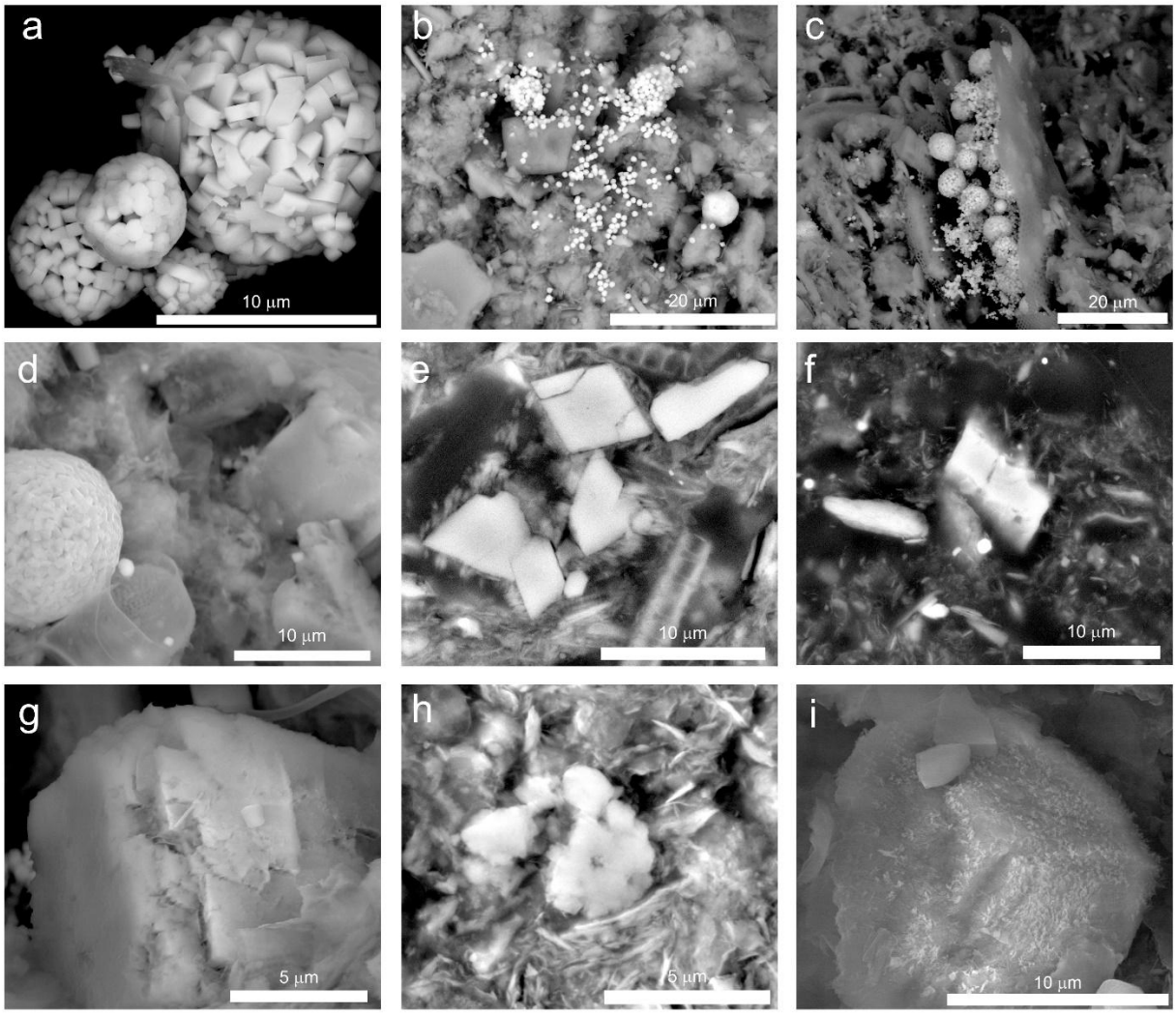

Figure 4: Examples of SEM-BSE images of authigenic sulfides and carbonates: (a) pyrite framboids, MET2 (40–45 cm); (b) pyrite framboid and disseminated pyrite crystals, ZGG (10¬–15 cm); (c) pyrite framboids within a diatom shell, ZGG (40–45 cm); (d) pyrite framboid, diatom, dolomite, MET1-MP (40–45 cm: thin section); (e) euhedral and subhedral dolomite crystals, MET1-MP (10¬–15 cm; thin section); (f) euhedral dolomite, MET1-MP (10¬–15 cm; thin section); (g) dolomite, MET1-MP (40¬–45 cm); (h) calcite surrounded by clay minerals, ZGG (40–45 cm); (i) siderite, MET2 (40–45 cm)

All sediments contain trace amounts of calcite ($CaCO_3$), occurring as fine (<10 μm) subhedral grains (Fig. 4h). Isolated euhedral siderite ($FeCO_3$) crystals were identified only at MET2 (Fig. 4i).

All Mössbauer spectra (Fig. S10; Table S4) are similar and dominated by Fe(II) components. The principal doublet, comprising ~50–60% of the spectral area, exhibits an isomer shift (IS) of ~0.3 mm s^{-1} and quadrupole splitting (QS) of ~0.6 mm s^{-1}. These parameters are characteristic of Fe(II) in pyrite (Byrne and Kappler, 2019). Two additional doublets contribute ~25–30% of the spectral area. They display high IS and QS values typical of Fe(II) in silicates (Dyar et al. 2006), although

those of the minority doublet are also similar to Fe(II) in siderite (Rothwell et al., 2025). A further doublet, accounting for ~10–28% of the spectral area, shows relatively low IS (~0.4–0.6 mm s^{-1}) and moderate QS (~0.7–0.9 mm s^{-1}). These parameters indicate high-spin Fe(III) in octahedral coordination. The precise mineral host of this component cannot be resolved. The hyperfine parameters are consistent with paramagnetic Fe(III) oxyhydroxides at room temperature (Byrne and Kappler, 2019). However, Fe(III) incorporated in phyllosilicates such as micas/illite, chlorites, or glauconite is also plausible (De Grave et al., 1987).

3.6 Burial rate of dolomite and pyrite

Carbonate burial rates were calculated using dolomite contents, as dolomite is the dominant carbonate phase. Pyrite burial rates were also determined due to pronounced inter-station variability. The highest dolomite burial occurs at MET1-MP (Table 2). Rates are 484 ± 13 µmol m^{-2} d^{-1} based on PXRD and 888 ± 87 µmol m^{-2} d^{-1} based on SEM–EDS. Intermediate values are observed at MET2 (254 ± 58 and 517 ± 7 µmol m^{-2} d^{-1}, respectively). The lowest rates occur at ZGG (60 ± 35 µmol m^{-2} d^{-1} from PXRD and 136 ± 110 µmol m^{-2} d^{-1} from SEM–EDS). In contrast, pyrite burial is highest at ZGG. Rates reach 959 ± 16 µmol m^{-2} d^{-1} (PXRD) and 1341 ± 87 µmol m^{-2} d^{-1} (SEM–EDS). At MET1-MP, values are 556 ± 18 and 640 ± 153 µmol m^{-2} d^{-1}, respectively. At MET2, pyrite burial rates are 341 ± 5 µmol m^{-2} d^{-1} (PXRD) and 785 ± 4 µmol m^{-2} d^{-1} (SEM–EDS).

4 Discussion

4.1 Typical anoxic sediment dominated by organoclastic sulfate reduction as the primary pathway of organic matter decomposition (station ZGG)

Nutrient enrichment associated with intensified fertilizer application has promoted widespread coastal eutrophication. Elevated nitrogen and phosphorus inputs stimulate primary production and increase the flux of OM to the seafloor. Enhanced organic carbon delivery raises sedimentary oxygen demand and promotes hypoxia and anoxia in bottom waters (Rabalais et al., 2010). These effects are amplified under strong density stratification, which limits vertical mixing and oxygen replenishment from surface layers (Carstensen et al., 2014). Under anoxic conditions, sulfate reduction becomes the dominant mineralization pathway, leading to hydrogen sulfide accumulation in bottom water.

Station ZGG, located in the western Gdańsk Deep in the southern Baltic Sea (Fig. S1), represents such an environment. The seafloor is covered by fine-grained sediments with mean water and OM contents of 76% and 11%, respectively, characteristic of an accumulation bottom type (Jönsson et al., 2005). TOC and TN values fall within the range typical for deep Baltic sediments (Uścinowicz, 2011). Maximum concentrations occur in the uppermost centimeters (Fig. 1a, b), reflecting enhanced eutrophication.

The molar TOC:TN ratio ranges from 8.5 to 11.8, exceeding typical marine values of 4–8 and indicating a contribution of terrestrial OM, for which TOC:TN commonly exceeds 12 (Meyers, 1997; Carneiro et al., 2021; Yadav et al., 2025). Carbon

isotopic compositions further support this interpretation. $\delta^{13}C$ values at ZGG range from −27.3‰ to −25.5‰ (Fig. 1e). These values are more negative than those of marine phytoplankton (−18‰ to −24‰; Yadav et al., 2025) and typical mid-latitude marine OM (−22‰ to −20‰; Meyers, 1994), and fall within the range characteristic of terrestrial C_3 plants (−35‰ to −25‰; average ~−27‰). The combined TOC:TN and $\delta^{13}C$ data indicate a significant input of vascular plant-derived organic carbon, which is carbon-rich and isotopically depleted relative to marine primary production (Meyers, 1994, 1997), in all the studied sediments. Riverine discharge is a major source of terrestrial carbon, contributing up to 10–30% of the total carbon pool in Baltic sediments (Miltner and Emeis, 2001). Nitrogen isotopic compositions ($\delta^{15}N$ = 2.0–3.6‰; Fig. 1f) are at or slightly below the typical range for marine OM (3–12‰; Maksymowska et al., 2000; Wada and Hattori, 1991). In contrast, terrestrial C_3 plants exhibit a broader range (−10‰ to +10‰). The relatively low $\delta^{15}N$ values at ZGG therefore further support a substantial allochthonous contribution. Increased biomass development may also lead to a modification of the isotopic composition of both nitrogen and carbon in sediments, the effect of which may also be visible in the case described. For example, a decrease in the $\delta^{15}N$ value of OM can be caused by the addition of isotopically light nitrogen to the N pool, bound by diazotrophic cyanobacteria, as in the case described by Struck et al. (2000) for the Gotland Basin. In turn, increased primary production can lead to an increase in ^{13}C content in sediment organic matter. For example, in the Oder Haff an increase of $\delta^{13}C$ in OM of 1.7 ‰ was found, while in the Gotland Basin it was 2.6 ‰ (Struck et al. 2000).

Sediments at ZGG are also characterized by elevated TS contents (1.59–3.58 wt%; Fig. 1c). The TOC:TS ratio provides insight into depositional redox and salinity conditions (Berner et al., 1979; Berner and Raiswell, 1984). A ratio of 2.8 ± 0.4 is typical of normal marine sediments underlying oxygenated waters (Berner, 1982). Lower values indicate enhanced sulfide formation under anoxic conditions, whereas TOC:TS > 2.8 is characteristic of freshwater environments. The mean TOC:TS ratio at ZGG (2.5 ± 0.6) is slightly lower below the marine oxic benchmark. This suggests suboxic to anoxic depositional conditions, controlled by substantial water depth, persistent stratification, and bottom-water oxygen depletion.

In the uppermost centimeters, pore-water composition closely resembles that of bottom water (Fig. 2). With increasing depth, diagenetic processes progressively modify the chemical composition. Sulfate concentrations decrease rapidly within the upper ~30 cm and stabilize at ~3.5 mmol dm^{-3} in deeper layers (Fig. 2d). In parallel, H_2S concentrations increase (Fig. 2e), reflecting active microbial sulfate reduction. Concentrations of NH_4^+, PO_4^{3-}, DIC, and TA also increase with depth (Fig. 3), indicating that a common mineralization process supplies these components to pore waters. Sulfate can be consumed during both OSR (Table S1: R5) and AOM (Table S1: R14). Although methanogenesis and AOM may occur deeper in the sediment at ZGG, sulfate remains relatively abundant throughout the studied profile, and CH_4 concentrations are below LOQ (Fig. 2f). These observations indicate that sampling captured the sulfate reduction zone above the sulfate–methane transition (SMT). This interpretation is consistent with the inhibitory effect of sulfate on methanogenesis, as sulfate-reducing microorganisms outcompete methanogens for H_2 and acetate (Reeburgh, 2007). The $\delta^{13}C$-DIC profile further supports this conclusion. $\delta^{13}C$-DIC values decrease with depth (Fig. 3c), whereas methanogenesis typically increases $\delta^{13}C$-DIC due to preferential removal of ^{12}C into CH_4 (Whiticar, 1999). Moreover, DIC and $\delta^{13}C$-DIC exhibit a strong linear correlation (R^2 = 0.98), and no $\delta^{13}C$-DIC minimum characteristic of the SMT is observed (Malinverno and Pohlman, 2011). The slope of the

464 regression corresponds to $\delta^{13}C$ values typical of marine OM (−22‰ to −20‰; Meyers, 1994), indicating that DIC is derived
465 predominantly from organic carbon oxidation (Chen et al., 2024).
466 These data demonstrate that OSR is the principal process consuming SO_4^{2-} and controlling pore-water DIC and TA at ZGG.
467 According to stoichiometry, OSR produces two moles of DIC per mole of sulfate reduced (Table S1: R5), whereas sulfate-
468 driven AOM yields a 1:1 ratio (Table S1: R14). The relationship between the increase in DIC (ΔDIC) and the decrease in
469 sulfate (ΔSO_4^{2-}) therefore provides a diagnostic criterion for distinguishing these processes (Masuzawa et al., 1992;
470 Rassmann et al., 2016). At ZGG, the $\Delta DIC:\Delta SO_4^{2-}$ ratio is 1.85:1 (Fig. S4), close to the theoretical 2:1 value expected for
471 OSR. Minor deviations from the theoretical ratio may reflect partial DIC removal by authigenic carbonate precipitation
472 (Akam et al., 2020). Chemoautotrophic CO_2 fixation may also contribute to DIC consumption (Treude et al., 2007). In
473 addition, a fraction of sediment-produced DIC diffuses into the overlying water. Assuming oxidation of H_2S at the sediment–
474 water interface, the estimated net diffusive benthic flux of carbonate alkalinity ($[HCO_3^-] + 2[CO_3^{2-}]$) and DIC at ZGG is 983
475 ± 40 and 942 μmol m^{-2} d^{-1}, respectively (Łukawska-Matuszewska and Kiełczewska, 2016; Łukawska-Matuszewska and
476 Dwornik, 2025).
477 The R_{OSR} values in ZGG sediments (24–46 μmol dm^{-3} d^{-1}) are consistent with rates reported from other Baltic regions using
478 radioisotope methods. These include 0.2–42.3 μmol dm^{-3} d^{-1} in the Curonian and Vistula Lagoons (Pimenov et al., 2013), 0–
479 43 μmol dm^{-3} d^{-1} in the Gdańsk Basin (Pimenov et al., 2010), and <1.0–21.4 μmol dm^{-3} d^{-1} in Kattegat (Iversen and
480 Jørgensen, 1985). The measured values also fall within the lower range of rates reported from Eckernförde Bay (10–465
481 μmol dm^{-3} d^{-1}; Treude et al., 2005), Himmerfjärden (0.2–338 μmol dm^{-3} d^{-1}; Sawicka and Brüchert, 2017), and the Gotland
482 Deep (<250 μmol dm^{-3} d^{-1}; Piker et al., 1998). Incubation-derived potential R_{OSR} values are several times higher than rates
483 previously calculated for the same area from sulfate pore-water gradients (0.2–4.6 μmol dm^{-3} d^{-1}; Łukawska-Matuszewska
484 and Dwornik, 2025). This discrepancy is expected, as incubation experiments determine gross sulfate reduction, whereas
485 pore-water profiles reflect net sulfate consumption (Iversen and Jørgensen, 1985). Experiments with labeled substrates in the
486 present study indicate the potential for AOM at ZGG (Table 1), with rates up to ~10 μmol dm^{-3} d^{-1}. This suggests that
487 methane could be oxidized if supplied from deeper layers. However, geochemical evidence indicates that the sampled
488 interval corresponds to the sulfate reduction zone above the SMT. Consequently, AOM does not significantly contribute to
489 DIC and TA production in the studied sediments. It should be also mentioned that experimentally-derived AOM rates
490 represent the potential activity of the microbial community under substrate-replete conditions rather than the actual in situ
491 process rates. Therefore, the similar experimentally-derived rates at MET-2 and ZGG indicate a comparable microbial
492 potential for AOM at both sites. In contrast, the porewater profiles reflect in situ conditions, where methane availability
493 differs substantially between the sites. At MET-2, methane is present and supports active AOM, which is reflected in the
494 porewater profiles. At ZGG, methane concentrations are negligible, so AOM appears less significant in situ despite the
495 presence of a microbial community capable of performing this process if methane became available.
496 Based on stoichiometry (Table S1: R5) and measured R_{OSR}, OSR contributes 49–92 μmol dm^{-3} d^{-1} of DIC to ZGG pore
497 waters. The depth-integrated DIC production from OSR within the 0–100 cm interval equals 54 mmol m^{-2} d^{-1} (Table 1).

Reduction of Mn(IV) during OM degradation may represent an additional DIC source, as indicated by the presence of Mn^{2+} in pore waters (Fig. 2g). However, Mn^{2+} concentrations are low relative to H_2S, the byproduct of sulfate reduction. Therefore, Mn(IV) reduction likely contributes only marginally to DIC production and is not included in the quantitative assessment. Besides Mn(IV) reduction, organic matter oxidation in marine sediments can proceed via denitrification. However, in the reducing sediments examined here nitrate was consistently below detection limit and nitrite occurred only at trace levels (data not shown), so denitrification was not quantified. While denitrification can produce DIC, we have no evidence for substantial availability of oxidized nitrogen species in these samples and therefore expect its contribution to be negligible.

The progressive increase in DIC with depth leads to pore-water supersaturation with respect to carbonate minerals, primarily calcite and dolomite, throughout most of the sediment column, except for the upper 5–10 cm (Fig. S11). Despite thermodynamic supersaturation, carbonate contents remain low (Table 2). Calcite occurs only in trace amounts, and dolomite was identified exclusively in the subsurface layer during summer. Moreover, anhedral morphology of many grains raises uncertainty as to whether all these carbonates are entirely authigenic. The dolomite burial rate is substantially lower than in methane-bearing sediments (Table 2) and does not exceed 271 μmol m^{-2} d^{-1}. For comparison, burial rates reach 525 μmol m^{-2} d^{-1} at MET2 and 994 μmol m^{-2} d^{-1} at MET1-MP. Comparable rates to those recorded at the ZGG - 60 ± 35 μmol m^{-2} d^{-1} from PXRD and 136 ± 110 μmol m^{-2} d^{-1} from SEM–EDS - were reported by Zha et al. (2022) for sediments on the northern slope of the South China Sea. Using reactive transport modeling, they estimated the burial rate of Ca-Mg carbonates to be 65 μmol^{-2} d^{-1} in the upper 30 cm of sediment at one site and 79 μmol^{-2} d^{-1} in the upper 10 cm at another.

The DIC:TA ratio is a simple diagnostic of the relative contribution of non-carbonate bases to total alkalinity. In seawater, DIC defined as the sum of $[CO_2^*]$ + $[HCO_3^-]$ + $[CO_3^{2-}]$ with $[CO_2^*]$ denoting the sum of dissolved $[CO_2]$ and $[H_2CO_3]$ (Dickson et al., 2007), typically represents over 95% of TA (Emerson and Hedges, 2008). In this concept, lower DIC:TA values signal a larger non-carbonate alkalinity fraction (e.g., HS^-, NH_3), whereas values near unity indicate TA is dominated by carbonate species. The mean DIC:TA ratio in ZGG pore waters is 0.75. This value indicates that approximately 25% of total alkalinity derives from non-carbonate bases, primarily H_2S. Hydrogen sulfide constitutes an independent acid–base system capable of proton exchange (Hu et al., 2010) and is therefore included in TA calculations. Upward diffusion of H_2S toward the sediment–water interface followed by oxidation leads to partial consumption of alkalinity (Table S1: R10) generated during anaerobic mineralization (Krumins et al., 2013). In contrast, precipitation of sulfides within the sediment (Table S1: R15) prevents complete reoxidation and results in a net increase in pore-water TA.

Geochemical modeling indicates that pore waters at ZGG are supersaturated with respect to iron sulfides, including greigite, mackinawite, and pyrite, throughout the sediment column (Fig. S11). Increasing TS content with depth and relatively low TOC:TS ratios further support enhanced sulfide accumulation compared to the methane-affected stations. Mineralogical data confirm that pyrite is more abundant at ZGG than at MET1-MP and MET2. Its burial rate ranges from 940 to 1447 μmol m^{-2} d^{-1}, several times higher than at the other sites, where OSR rates and pore-water H_2S concentrations are lower. These values

are high and comparable to the upper range reported by Jørgensen et al. (1990) for sediments from the Baltic–North Sea transition zone (50–1240 μmol m^{-2} d^{-1}).

The rate of sulfate reduction in the studied sediments likely exceeds the rate of reaction between H_2S and reactive iron phases. This imbalance promotes the accumulation of dissolved H_2S in pore waters (Boesen and Postma, 1988; Canfield et al., 1992). Accordingly, H_2S concentrations remain high throughout the sediment profile, whereas Fe^{2+} is largely depleted from pore waters (Fig. 2). Mössbauer spectroscopy indicates that iron is predominantly divalent (Fig. S10). Thus, the availability of reactive Fe(III) phases likely limits pyrite formation. Such limitation is typical of anoxic to euxinic marine environments (Raiswell and Berner, 1985; Boesen and Postma, 1988) and has previously been documented for sediments of the Gdańsk Deep (Łukawska-Matuszewska et al., 2019). Incomplete removal of H_2S as solid sulfides and its reoxidation (Table S1: R10) may contribute to pore-water acidification. The observed increase in Ca^{2+} concentration with depth (Fig. 2) may therefore reflect carbonate dissolution driven by lowered pH.

4.2 Nearshore methane-bearing sediment with high terrigenous organic matter input (station MET2)

High OM loading from local primary production and terrigenous sources increases oxygen demand in coastal sediments and frequently exceeds oxygen supply (Hedges et al., 1997; Schlünz and Schneider, 2000). Oxygen penetration is therefore shallow. It is typically <1 mm in muddy and silty sediments and only a few centimeters in sands (Glud, 2008), owing to limited transport and rapid consumption. As a consequence, anaerobic mineralization dominates in most coastal settings (Soetaert et al., 1996), with sulfate serving as the principal electron acceptor, as observed at station ZGG. When organic carbon input exceeds sulfate availability, mineralization proceeds via methanogenesis (Froelich et al., 1979). Diagenetic zonation in coastal sediments differs markedly from that in open-ocean environments. Redox zones are thinner and shifted closer to the sediment surface (D'Hondt et al., 2004; Egger et al., 2018). In low-salinity settings, sulfate reduction, the SMT, and methanogenesis commonly occur at shallow depths (Albert et al., 1998; Thang et al., 2013; Egger et al., 2015). Station MET2 is located in a nearshore zone (Fig. S1) with bottom-water salinity of ~7–8. The molar TOC:TN ratio (9.3–13.7; Fig. 1d) indicates a substantial contribution of terrestrial OM, which is relatively nitrogen-poor compared to protein-rich marine phytoplankton. Carbon isotopic compositions support this interpretation. $\delta^{13}C$ values range from −26.0‰ to −24.4‰, i.e., below −24‰, consistent with terrestrial input (Yadav et al., 2025). Nitrogen isotopic values ($\delta^{15}N$ = 1.21–6.66‰) show the greatest ^{15}N enrichment in the upper 0–20 cm, coinciding with elevated TOC and TN contents. Terrestrial OM is generally less degradable than marine OM due to the abundance of cellulose and lignin in vascular plant tissues (Dickens et al., 2006). The observed isotopic and compositional variations therefore reflect preferential degradation of labile phytoplankton-derived compounds and the relative accumulation of more refractory terrestrial material in the sediment.

Because MET2 is located in a shallower, transport-dominated setting, the sediment consists of sandy silt and contains lower TOC and TN than the silty and clayey sediments at the other stations (Fig. 1a, b). Owing to the relatively low salinity, major ion concentrations in bottom and pore waters are the lowest among all sites. These concentrations remain nearly constant with depth, except for SO_4^{2-} (Fig. 2a–d). Sulfate decreases rapidly within the upper 0–40 cm due to microbial reduction and

falls below LOQ at greater depths. In the upper ~20 cm bsf, the $\Delta DIC:\Delta SO_4^{2-}$ ratio ranges from 1.0 to 2.1, consistent with contributions from both sulfate-driven AOM and OSR. The mean ratio of 1.51:1 indicates a mixed origin of DIC. Below this interval, DIC production becomes disproportionately high relative to sulfate consumption, and the $\Delta DIC:\Delta SO_4^{2-}$ ratio increases to ~4.0 (Fig. S4). Such excess DIC may reflect processes that produce DIC but do not consume sulfate, including methanogenesis, or alternative AOM pathways coupled to Mn(IV) or Fe(III) reduction (Meister et al., 2019). Elevated Mn^{2+} concentrations between 30 and 80 cm and Fe^{2+} below 80 cm (Fig. 2g, h) may suggest involvement of these pathways. However, the absolute concentrations of Mn^{2+} and Fe^{2+} are low, indicating that metal-driven AOM likely contributes only marginally to DIC and TA production and is not considered further.

Methane concentrations at MET2 reach 6.5 mmol dm^{-3} in summer and 8.45 mmol dm^{-3} in winter (Fig. 2f). Stable isotope data for $\delta^{13}C\text{-}CH_4$, $\delta^{2}H\text{-}CH_4$, and $\delta^{13}C\text{-}CO_2$ (Fig. 5) indicate a microbiological origin, predominantly via hydrogenotrophic methanogenesis (Whiticar, 1999). Methane concentrations decrease upward from maxima in deeper layers to values below LOQ in the uppermost centimeters. Methane is absent from the overlying water column, demonstrating that the sediment acts as an efficient methane filter despite the shallow SMT at ~5–13 cm bsf. In Baltic Sea sediments, SMT depths vary widely, ranging from 80–160 cm in the Danish Straits (Iversen and Jørgensen, 1985), ~150 cm in Aarhus Bay (Thomsen et al., 2001), and 30–40 cm in the Gotland Deep (Piker et al., 1998). SMT depths comparable to those observed here have been reported from Storfjärden and Pojo Bay (Myllykangas et al., 2020; Jilbert et al., 2021), the western Gotland Basin (Ketzer et al., 2024), and Eckernförde Bay in the southwestern Baltic Sea (Treude et al., 2005; Maltby et al., 2018).

The occurrence of sulfate-dependent AOM within the 5–13 cm bsf interval is indicated by the most negative $\delta^{13}C$-DIC values (Fig. 3c) (Malinverno and Pohlman, 2011). In the overlying sediment, OM is oxidized primarily via OSR. However, separation of OSR and AOM zones based solely on isotopic data is difficult, as both processes produce ^{13}C-depleted DIC. OSR shifts $\delta^{13}C$-DIC from values near 0‰, typical of seawater, toward approximately −21‰, characteristic of marine OM. Subsequent sulfate-driven AOM may further deplete DIC in ^{13}C through oxidation of isotopically light CH_4 (Meister and Reyes, 2019). At MET2, $\delta^{13}C$-DIC values range from −12.7‰ to −1.2‰. These values are markedly less negative than expected for only AOM or OSR end-members. If DIC generated by sulfate-AOM inherited the isotopic signature of methane entering the SMT, $\delta^{13}C$-DIC values would approach ~−76‰. Conversely, DIC derived from OSR should approximate the $\delta^{13}C$ of sedimentary OM (−25.6‰ at MET2). The relatively enriched $\delta^{13}C$-DIC values observed in both AOM and OSR intervals suggest mixing with ^{13}C-enriched DIC diffusing upward from the methanogenic zone (Malinverno and Pohlman, 2011; Meister and Reyes, 2019). Overall, pore-water DIC at MET2 reflects a mixture of inorganic carbon produced by overlapping diagenetic processes. A comparable situation has been reported from Storfjärden, where OSR, sulfate-driven AOM, and methanogenesis co-occur within compressed redox zones (Jilbert et al., 2021).

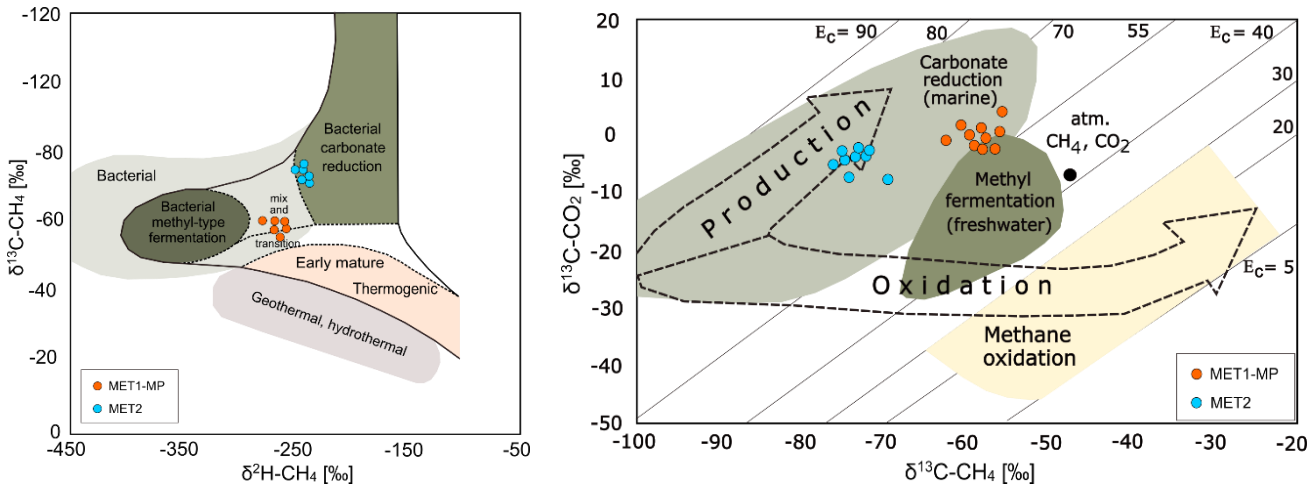

Figure 5: Origin of methane inferred from the combined $\delta^{13}C$ and $\delta^{2}H$ composition of methane (a) and from $\delta^{13}C$ values of methane and carbon dioxide (b) in sediments at stations MET1-MP and MET2 in the Gdańsk Basin (modified after Whiticar, 1999).

The R_{OSR} values at MET2 range from 21 to 48 µmol dm^{-3} d^{-1}. These rates are comparable to those measured at the other stations (Table 2) and fall within ranges reported in the literature (Sect. 4.1). The R_{AOM} values (6–33 µmol dm^{-3} d^{-1}) are also consistent with data from other Baltic regions, including 0–50 µmol dm^{-3} d^{-1} in the Gdańsk Basin (Pimenov et al., 2010), 0.03–14 µmol dm^{-3} d^{-1} in Eckernförde Bay (Treude et al., 2005), and 0.002–6.2 µmol dm^{-3} d^{-1} in Kattegat and Skagerrak (Iversen and Jørgensen, 1985). The highest R_{AOM} occurs within the 0–20 cm layer. Rates in this interval are up to six times higher than those in the 20–40 cm layer. This distribution corresponds to geochemical indicators, including the steepest SO_4^{2-} gradient, maximum H_2S concentrations, $\Delta DIC:\Delta SO_4^{2-}$ ratios lower than expected exclusively for OSR, and negative $\delta^{13}C$-DIC values in the upper sediment. At MET2, R_{OSR} contributes 41–96 µmol DIC dm^{-3} d^{-1} to pore waters. The depth-integrated DIC production from OSR within the 0–100 cm interval equals 59 mmol m^{-2} d^{-1}, similar to values obtained for ZGG (Table 1). In addition, AOM contributes 6–33 µmol dm^{-3} d^{-1} of DIC, corresponding to an integrated production rate of 9 mmol m^{-2} d^{-1}. The pronounced chemical gradients at the sediment–water interface correspond to a diffusive benthic flux of carbonate alkalinity ($[HCO_3^-] + 2[CO_3^{2-}]$) estimated at 1498 ± 80 µmol m^{-2} d^{-1} (Łukawska-Matuszewska and Dwornik, 2025). The mean DIC:TA ratio in MET2 pore waters is 0.97. This value indicates a relatively minor contribution of non-carbonate bases to total alkalinity compared to ZGG. The dominance of carbonate alkalinity suggests that alkalinity production at MET2 is less reversible. In contrast, at ZGG, substantial H_2S production and its subsequent oxidation release H^+ and partially consume alkalinity (Table S1: R10).

Pore waters at MET2 exhibit higher saturation indices with respect to calcite and dolomite than those at methane-free ZGG (Fig. S11). Intense diagenesis leads to a strong increase in DIC, which raises porewater saturation with respect to carbonates and thereby promotes precipitation of authigenic phases. This is consistent with the greater abundance of dolomite throughout the sediment column, as documented by PXRD and microscopic observations (Table 2). The dolomite burial rate at MET2 (184–525 µmol m^{-2} d^{-1}) substantially exceeds that at ZGG (1–271 µmol m^{-2} d^{-1}). Taken together, the porewater

chemistry and burial rates suggest that methane-bearing sediments in our study area sequester more inorganic carbon than methane-free, OSR-dominated sediments (ZGG) - likely because methane-related processes generate additional DIC.

In deeper layers at MET2, pore waters are also supersaturated with respect to siderite. In contrast, siderite is undersaturated throughout the ZGG profile (Fig. S11). This difference likely reflects Fe^{2+} availability. At ZGG, Fe^{2+} is efficiently removed from pore waters through reaction with abundant H_2S and subsequent sulfide precipitation. At MET2, H_2S is restricted to a narrow interval, with maximum concentrations at ~13 cm bsf (Fig. 2e). Below this depth, H_2S concentrations fall below LOQ. Under these conditions, a fraction of dissolved Fe^{2+} may precipitate as siderite rather than as iron sulfides.

In MET2 sediments, the mean TOC:TS ratio is 2.8. This value corresponds to typical marine sediments deposited beneath oxygenated bottom waters (Berner, 1982). Under such conditions, H_2S required for pyrite formation is produced within the anaerobic sediment during OM degradation. The rate of FeS_2 formation is controlled primarily by sedimentation rate and organic matter supply (Berner, 1982).

In contrast, at ZGG, H_2S frequently occurs in the overlying water column. This allows pyrite to form not only within the sediment but also in the water column (Raiswell and Berner, 1985) and, as a result, pyrite is more abundant at ZGG than at MET2 (Table 2). At MET2, the pyrite burial rate ranges from 334 to 789 μmol m^{-2} d^{-1}, the lowest among the studied sites. This reflects oxygenated bottom waters and comparatively low H_2S concentrations in pore waters. These conditions likely explain the Mössbauer results, which show a slightly lower proportion of Fe(II) associated with pyrite in the upper sediment layers at MET2 compared to deeper layers and to the other stations (Table S4).

4.3 Sediment affected by freshwater infiltration and methanogenesis (pockmark MET1-MP)

Sedimentation rate and organic carbon burial strongly regulate sulfate consumption and the depth of the SMT in marine sediments (Canfield, 1991; Egger et al., 2018). In coastal settings, submarine groundwater discharge (SGD) constitutes an additional controlling factor. SGD involves the exchange of terrestrial groundwater mixed with recirculated seawater that has infiltrated coastal aquifers. Its chemical composition often deviates from conservative mixing due to biogeochemical reactions within the aquifer (Moore, 2010). In the Gdańsk Basin, SGD occurs in both coastal and deeper offshore areas. It is expressed by anomalous salinity distributions, with lower salinity in bottom and pore waters relative to the overlying water column (Piekarek-Jankowska et al., 1994; Falkowska and Piekarek-Jankowska, 1999; Ehlert von Ahn et al., 2024; Matciak et al., 2024). In nearshore zones, SGD significantly affects water quality by supplying carbon, nutrients, and contaminants (Szymczycha et al., 2012, 2013, 2023). However, station MET1-MP, located in central Gulf of Gdańsk ~80 m water depth, represents a deepwater pockmark where freshwater originates from the Upper Cretaceous aquifer beneath the seafloor (Kozerski et al., 1987). Fresh groundwater infiltration into the pockmark has been documented previously (Brodecka-Goluch et al., 2022) and is confirmed here by the Cl^- profile in pore waters (Fig. 2a). The inflow of freshwater dilutes pore waters and reduces SO_4^{2-} availability for OM and methane oxidation. This alteration of sulfate supply modifies early diagenetic processes and promotes shallow methanogenesis (Pimenov et al., 2010; Ehlert von Ahn et al., 2024).

As a seabed depression formed by gas expulsion, this pockmark acts as a natural sediment trap. It accumulates both autochthonous and allochthonous OM. Consequently, silty sediments at MET1-MP exhibit the highest TOC and TN concentrations among the studied sites (Fig. 1a, b). The TOC:TN ratio (7.8–8.7) approaches that typical of marine OM. However, the isotopic composition of carbon and nitrogen in the organic fraction (Fig. 1e, f) indicates an additional contribution of terrestrial material.

The pockmark's physical and sedimentary characteristics concentrate OM, raising demand for electron acceptors and fueling intense diagenesis; as a result, porewater sulfate is rapidly consumed in the uppermost decimeters and the sulfate–methane transition shifts toward the sediment surface. Methanogenesis and AOM supply additional DIC alongside OSR, causing elevated porewater DIC through intense diagenesis. Pore waters at MET1-MP are also characterized by very high concentrations of NH_4^+ and PO_4^{3-} (Fig. 3d, e). These elevated nutrient levels further indicate intense degradation of the substantial OM inventory accumulated within the pockmark sediments.

The substantial water depth and persistent stratification at MET1-MP further constrain oxygen supply to the sediment, similar to conditions at ZGG. Under these conditions, SO_4^{2-} is rapidly depleted from pore waters. The SMT is extremely shallow. The δ^{13}C-DIC profile (Fig. 3c) indicates that the SMT center is located immediately below the sediment surface, likely within 3–5 cm bsf. Within the upper ~8 cm, $\Delta DIC:\Delta SO_4^{2-}$ ratios reflect contributions from OSR, AOM, or both processes. The mean ratio of 1.24:1 suggests that sulfate-driven AOM plays a dominant role in SO_4^{2-} consumption in this interval (Miller et al., 2017). At greater depths, ΔDIC values exceed those expected from OSR and AOM, indicating an additional DIC source unrelated to SO_4^{2-} consumption. With increasing depth, δ^{13}C-DIC shifts toward positive values, reaching up to +16.4‰ (Fig. 3c). Similar values (up to +14‰) and comparable pore-water profiles were reported by Ehlert von Ahn et al. (2024) from a station located in similar area. This enrichment likely reflects the upward diffusion of ^{13}C-enriched DIC generated during methanogenesis, as observed at MET2. However, groundwater infiltration may also contribute.

Groundwaters from the Upper Cretaceous aquifer in the Gdańsk region are predominantly of the HCO_3–Na and HCO_3–Ca types (Sadurski, 1985). They are alkaline (pH 7.5–8.3) and exhibit variable dissolved solute concentrations, with DIC values reaching ~11 mmol dm^{-3} (Kozerski et al., 1987). These waters circulate through glauconitic sands forming the principal aquifer and migrate upward through carbonate and siliceous strata, including carbonates, gaizes, and marls (Sadurski, 1985). Infiltrating groundwater can dilute pore waters and reduce DIC concentrations in deeper sediment layers (Fig. 3b). Moreover, groundwater DIC is commonly enriched in ^{13}C due to carbonate dissolution and isotopic exchange with $CaCO_3$, for which δ^{13}C values typically exceed 0‰ (Walter et al., 2007; Han et al., 2014; Campeau et al., 2017). Consequently, both methanogenesis and SGD influence the δ^{13}C-DIC signature in pore waters of the MET1-MP pockmark.

Stable isotope data indicate that CH_4 at MET1-MP is of microbiological origin (Fig. 5). Methane is generated not only by CO_2 reduction but also by acetate fermentation, a pathway commonly associated with freshwater environments (Whiticar, 1999; Batther et al., 2025). This dual signature further demonstrates the influence of freshwater infiltration on sedimentary microbial processes. In contrast to MET2, where CH_4 concentrations increase progressively with depth, the MET1-MP

profile exhibits a subsurface or intermediate maximum (Fig. 2f). The extremely shallow SMT and the occurrence of methane close to the sediment surface may enhance the potential for gas escape into the water column. Lapham et al. (2024) showed that methane leakage across the SMT is widespread in organic-rich Baltic Sea sediments, with a highly variable amount of subseafloor gas escaping oxidation (0–100%). Previous investigations documented gas emissions from multiple locations within the MET1-MP pockmark (Brodecka et al., 2013; Majewski and Klusek, 2014; Łukawska-Matuszewska et al., 2025). The pockmark is a large structure (~1200 m long and ~500 m wide), and gas discharge is spatially heterogeneous. Fluid migration pathways and rates vary considerably. During the present study, CH_4 concentrations in bottom water were below LOQ, whereas surface sediments contained ~0.3 mmol dm^{-3} CH_4. Thus, diffusion into bottom water followed by aerobic oxidation cannot be excluded.

The R_{OSR} attains a maximum of 164 µmol dm^{-3} d^{-1} in the 0–20 cm layer. This peak corresponds to steep SO_4^{2-} depletion and elevated H_2S concentrations, reflecting active sulfate reduction. Below 20 cm, R_{OSR} decreases markedly and remains relatively uniform across deeper layers (Table 2). Excluding the surface interval, R_{OSR} is lower than at the other stations. In contrast, R_{AOM} is substantially higher, ranging from 59 to 1077 µmol dm^{-3} d^{-1}. These R_{AOM} values exceed most rates reported for the Baltic Sea. Rates measured in the 0–20 cm, 20–40 cm, and 60–80 cm layers are comparable to those reported by Pimenov et al. (2008), who observed a maximum of 80.6 µmol dm^{-3} d^{-1} in another gas-saturated pockmark in the Gdańsk Basin, among the highest previously documented in the region. By comparison, AOM rates in Eckernförde Bay range from 0.03 to 14 µmol dm^{-3} d^{-1} (Treude et al., 2005), in the Curonian and Vistula Lagoons from 0.07 to 2.89 µmol dm^{-3} d^{-1} (Pimenov et al., 2013), and in Kattegat and Skagerrak from 0.002 to 6.2 µmol dm^{-3} d^{-1} (Iversen and Jørgensen, 1985). The highest R_{AOM} values at MET1-MP approach those reported for gassy sediments at a cold seep in Monterey Bay (280 ± 40 µmol dm^{-3} d^{-1}) and fall within the lower range measured at a cold seep in the Gulf of Mexico, where rates reached 4800 ± 400 µmol dm^{-3} d^{-1} (Bowles et al., 2019).

Direct comparison of microbial rates among studies remains challenging: even when identical radiotracer protocols are used, variability in microbial community structure, sediment properties and incubation conditions can produce substantially different rate estimates. At MET1-MP, R_{AOM} varies by up to two orders of magnitude between sediment layers. Comparable intra-profile variability has been documented elsewhere in the Baltic Sea (e.g., Iversen and Jørgensen, 1985; Pimenov et al., 2008; Pimenov et al., 2013), where rates differed by as much as 300% among layers. Nevertheless, the MET1-MP pockmark exhibits a markedly greater AOM capacity than the other sites investigated in this study and than most previously studied Baltic sediments. Depth-integrated calculations demonstrate that AOM is the dominant DIC source at MET1-MP. OSR contributes 58 mmol m^{-2} d^{-1} of DIC, whereas AOM supplies 331 mmol m^{-2} d^{-1}, more than five times greater. Consistently, MET1-MP represents the strongest benthic DIC source among the studied sites. The estimated net diffusive flux of carbonate alkalinity equals 2017 ± 47 µmol m^{-2} d^{-1} (Łukawska-Matuszewska and Dwornik, 2025), exceeding fluxes from the other sediments by 50–100%.

Intense DIC production within the MET1-MP pockmark results in markedly elevated DIC and TA concentrations relative to the other stations (Fig. 3a, b). In contrast to MET2 and ZGG, however, DIC does not increase progressively with depth.

Below ~30 cm, DIC concentrations decline. This pattern may partly reflect dilution by infiltrating freshwater. Because the exact chemical composition of the discharging waters is not fully constrained, their quantitative influence on DIC variability cannot be assessed. Notably, the decrease in DIC coincides with pronounced declines in Mg^{2+} and Ca^{2+} concentrations (Fig. 2b, c). This relationship suggests that authigenic carbonate precipitation represents an additional controlling process. Comparable pore-water trends have been reported from methane-affected settings, including shallow sediments of the western slope of the Mid-Okinawa Trough (Xu et al., 2018), pockmark sediments of the Northern Congo Fan (Nöthen and Kasten, 2011), and pockmarks on the inner shelf of the East China Sea (Wang et al., 2024).

Among the studied sites, MET1-MP affected by methanogenesis and freshwater infiltration exhibits the highest average dolomite content. Euhedral crystals are common, supporting an authigenic origin. In addition to dolomite and minor calcite, traces of siderite were identified. Authigenic carbonate formation at MET1-MP therefore constitutes an efficient inorganic carbon sink. This observation is consistent with Rzepa et al. (in press), who found that freshwater input in another deepwater pockmark in the Gdańsk Basin lowers porewater sulfate and promotes methanogenesis and Fe-mediated AOM, increasing dissolved inorganic carbon and thereby favoring authigenic carbonate formation. The dolomite burial rate ranges from 467 to 994 $\mu mol\ m^{-2}\ d^{-1}$, substantially exceeding values at ZGG (1–271 $\mu mol\ m^{-2}\ d^{-1}$) and MET2 (184–525 $\mu mol\ m^{-2}\ d^{-1}$). Similarly, Chen et al. (2024) found that at the Makran continental margin, sediments with a high methane flux exhibited authigenic carbonate precipitation rates that were at least double those of the background area.

In the MET1-MP pockmark influenced by freshwater infiltration, the effect of CH_4 on redox-sensitive elements (Fe and Mn) is more pronounced than at MET2. Freshening and reduced sulfate availability enhance the relative importance of alternative methane oxidation pathways (Egger et al., 2015). The observed increase in Fe^{2+} and Mn^{2+} concentrations below the sulfate reduction zone likely reflects reductive dissolution of Fe(III) and Mn(IV) phases coupled to AOM. The measured R_{AOM} values probably include contributions from both sulfate-dependent AOM and metal-dependent AOM, provided that microorganisms capable of these pathways were present. This distinction does not affect DIC production estimates, as oxidation of 1 mol of CH_4 yields 1 mol of HCO_3^- irrespective of the terminal electron acceptor (Table S1:R12-R14). MET1-MP exhibits the highest Fe^{2+} concentrations among the studied stations. This contrasts with ZGG, where Fe^{2+} is almost entirely removed from pore waters through reaction with abundant H_2S. The total sulfur content in MET1-MP sediments is lower than at ZGG, and the TOC:TS ratio is several times higher (Fig. 1). These relations indicate that H_2S availability limits pyrite formation in sediments influenced by freshwater infiltration. Despite this limitation, pyrite remains a common authigenic phase at MET1-MP. However, its mean concentration is significantly lower than at ZGG. The pyrite burial rate ranges from 453 to 828 $\mu mol\ m^{-2}\ d^{-1}$, comparable to values at MET2. These rates are approximately half those observed at ZGG, where intense sulfate reduction promotes high H_2S production and enhanced iron sulfide precipitation.

5 Conclusions

This comparative study of shelf sediments highlights the complexity of diagenetic processes controlled by local environmental conditions and their implications for the carbon cycle. It demonstrates that the function of sediments as sources or sinks of inorganic carbon varies in response to redox regime, methane dynamics, sulfate availability, and freshwater input. Our synthesis shows that carbonate dynamics are governed by interactions among OSR, methanogenesis, AOM, sulfate supply, and freshwater input (Fig. 6). Recognition of these coupled processes is essential for predicting sedimentary carbon cycling under changing environmental conditions and for refining current models of carbonate dynamics in shelf environments.

Methane-bearing sediments differ markedly from anoxic sediments dominated solely by OSR. In the latter, DIC production is approximately 40% lower, based on the sites studied. Where OM supply exceeds sulfate availability, methanogenesis and the coupled AOM become important additional sources of DIC in pore waters, contributing to the elevated DIC levels observed in methane-bearing sediments. Sediments in which both OSR and AOM operate release substantially more inorganic carbon to the overlying water. Benthic fluxes are 50–100% higher than in sediments lacking active methanogenesis. The role of methane-related processes becomes increasingly important in sediments influenced by freshwater input, where the SMT is shallower and AOM can be a principal DIC source relative to OSR. AOM - particularly where freshwater inflow reduces sulfate availability - supplies additional DIC that contributes to carbonate supersaturation; this favors authigenic carbonate formation, which can act as an important inorganic-carbon sink.

To our knowledge, this study provides the first quantitative estimate of authigenic carbonate burial rates in Baltic Sea sediments. Overall, the results demonstrate that anaerobic methane oxidation can play a significant role in regulating authigenic carbonate burial and, consequently, seawater chemistry.

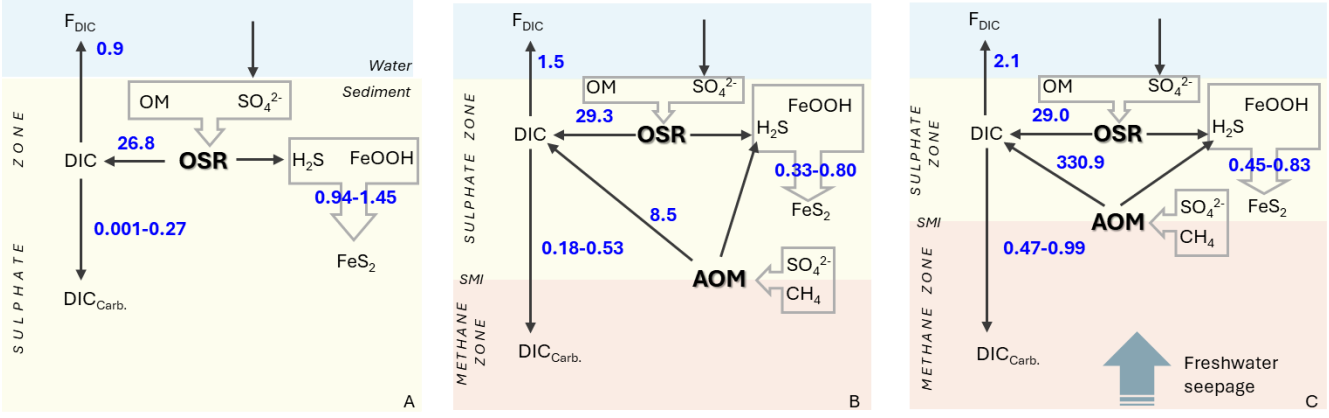

Figure 6: Simplified conceptual model of inorganic carbon cycling in shelf sediments under contrasting environmental settings: (A) anoxic sediments dominated by organoclastic sulfate reduction as the principal pathway of organic matter oxidation; (B) nearshore sediments characterized by substantial terrigenous organic matter input and active methanogenesis; and (C) sediments influenced by freshwater infiltration and methanogenesis. Abbreviations: OSR – organoclastic sulfate reduction; AOM – anaerobic oxidation of methane; OM – organic matter; DIC – dissolved inorganic carbon in pore water; F_{DIC} – diffusive benthic

DIC flux (after Łukawska-Matuszewska and Dwornik, 2025); $DIC_{carb.}$ – burial of authigenic carbonate (dolomite). Numerical values represent fluxes and depth-integrated rates of DIC production and consumption associated with individual processes, expressed in mmol m^{-2} d^{-1}.

Data availability

The original data presented in the study are included in the article/Supplementary Material; further inquiries can be directed to the corresponding author.

Supplement link

Supplement of "Biogeochemical controls on carbonate dynamics driven by methane and freshwater inputs in shallow sediments of a brackish continental shelf sea"

Author contributions

KŁM: Writing (original draft preparation); Writing (review and editing); Conceptualization; Investigation; Validation; Formal analysis; Visualization; Project administration; Supervision. GRz: Writing (original draft preparation); Writing (review and editing); Investigation; Validation; Formal analysis; Visualization; Project administration; Supervision. ABG: Investigation; Writing (original draft preparation); Writing (review and editing); AB: Investigation; Methodology; Writing (original draft preparation); Writing (review and editing); BG-Cz: Writing (original draft preparation); Writing (review and editing); Investigation. AB: Writing (original draft preparation); Writing (review and editing); Investigation; Formal Analysis. MM: Writing (original draft preparation); Writing (review and editing); Formal Analysis. JK: Formal analysis; Visualization. MD: Methodology; Formal analysis; Data Curation. MR: Investigation..

Competing interests

The authors declare that they have no conflict of interest.

Acknowledgements

The authors would like to thank the captains and the crew of r/v Oceanograf.

Financial support

The authors declare that financial support was received for the research and/or publication of this article. The study was funded by the National Science Centre, Poland (grant number 2022/45/B/ST10/00395).

References

Akam, S.A., Coffin, R.B., Abdulla, H.A.N., Lyons T.W.: Dissolved Inorganic Carbon Pump in Methane-Charged Shallow Marine Sediments: State of the Art and New Model Perspectives, Front. Mar. Sci., 7, 206, https://doi.org/10.3389/fmars.2020.00206, 2020.

Albert, D. B., Martens, C. S., Alperin, M. J.: Biogeochemical Processes Controlling Methane in Gassy Coastal Sediments-Part 2: Groundwater Flow Control of Acoustic Turbidity in Eckernförde Bay Sediments, Continental Shelf Res., 18, 1771–1793, doi:10.1016/S0278-4343(98)00057-0, 1998.

Alves, J.F., Edwards, H.G.M., Korsakov, A., Cappa de Oliveira, L.F.C.: Revisiting the Raman Spectra of Carbonate Minerals. Minerals, 13, 1358. https://doi.org/10.3390/min13111358, 2023.

Baker, P.A., Burns, S.J.,: Occurrence and Formation of Dolomite in Organic-Rich continental Margin Sediments. AAPG Bull., 69, 1917–1930, doi:10.1306/94885570-1704-11d7-8645000102c1865d, 1985.

Bauer, J.E., Cai, W-J., Raymond, P.A., Bianchi, T.S., Hopkins, Ch.S., Regnier, P.A.G.: The changing carbon cycle of the coastal ocean, Nature, 504, 61–70, https://doi.org/10.1038/nature12857, 2013.

Batther, H.K., Templeton, A.S., Hoehler, T., Howells, A., Bill, M., Gropp, J., Kopf, S.: The stable carbon isotope fractionation of methanogenesis products at complete carbon consumption, Geochemical Perspectives Letters, 37, 35-39. 10.7185/geochemlet.2543, 2025.

Berner, R.A.: Burial of organic carbon and pyrite sulfur in the modern ocean: its geo-chemical and environmental significance, American Journal of Science, 282, 451–473, https://doi.org/10.2475/ajs.282.4.451, 1982.

Berner, R.A., Raiswell, R.: C/S method for distinguishing freshwater from marine sedimentary rocks, Geology, 12, 365–368, https://doi.org/10.1130/0091-7613(1984)12<365:CMFDFF>2.0.CO;2; 1984.

Berner, R.A., Baldwin, T., Holdren, G.R.: Authigenic iron sulfides as paleosalinity indicators, J Sediment Res, 49, 1345–1350, https://doi.org/10.1306/212F7923-2B24-11D7-8648000102C1865D, 1979.

Błachowski, A., Ruebenbauer, K., Żukrowski, J., Górnicki, R.: Early design stage of the MsAa-4 Mössbauer spectrometer, Acta Phys. Pol. A, 114, 1707–1713, https://doi.org/10.12693/APhysPolA.114.1707, 2008.

Boesen, C., Postma, D.: Pyrite formation in anoxic environments of the Baltic, Am J Sci, 288, 575–603, https://doi.org/10.2475/ajs.288.6.575, 1988.

Boetius, A., Ravenschlag, K., Schubert, C. J., Rickert, D., Widdel, F., Gieseke, A., Amann, R., Jørgensen, B.B., Witte, U., Pfannkuche, O.: A marine microbial consortium apparently mediating anaerobic oxidation of methane, Nature 407, 623–626, https://doi.org/10.1038/35036572, 2000.

831 Brodecka, A., Majewski, P., Bolałek, J., Klusek, Z.: Geochemical and acoustic evidence for the occurrence of methane in
832 sediments of the Polish sector of the southern Baltic Sea, Oceanologia, 55, 951–978, https://doi.org/10.5697/oc.55-4.951,
833 2013.
834 Budrige, D.J.: Estuarine and coastal sediments – coupled biogeochemical cycling. Treatise, Estuar. Coast. Sci., 5, 279-316,
835 https://doi.org/10.1016/B978-0-12-374711-2.00511-8, 2011.
836 Byrne, J.M., Kappler, A.: Mössbauer spectroscopy, in: Analytical Geomicrobiology. A Handbook of Instrumental
837 Techniques, edited by: Kenney, J.P.L., Veeraramani, H., Alessi, D.S., Cambridge University Press, pp. 314–337, 2019.
838 Cai W.-J.: Estuarine and Coastal Ocean Carbon Paradox: CO_2 sinks and sites of terrestrial carbon incineration? Annu. Rev.
839 Mar. Sci., 3, 123-145, https://doi.org/10.1146/annurev-marine-120709-142723, 2011.
840 Campeau, A., Wallin, M.B., Giesler, R., Löfgren, S., Mörth, C-M., Schiff, S., Vekiteswaran, J.J., Bishop, K.: Multiple
841 sources and sinks of dissolved inorganic carbon across Swedish streams, refocusing the lens of stable C isotopes, Sci Rep, 7,
842 9158, https://doi.org/10.1038/s41598-017-09049-9, 2017.
843 Carneiro, M.L., Zucchi, M., Bomfim de Jesus, T., Junior, J., Hadlich, G.: δ13C, δ15N and TOC/TN as indicators of the
844 origin of organic matter in sediment samples from the estuary of a tropical river, Marine Pollution Bulletin, 172, 112857,
845 10.1016/j.marpolbul.2021.112857, 2021.
846 Canfield, D.E.: Sulfate Reduction in Deep-Sea Sediments, Am. J. Sci., 291, 177–188, https://doi.org/10.2475/ajs.291.2.177,
847 1991.
848 Canfield, D.E., Raiswell, R., Bottrell, S.H.: The reactivity of sedimentary iron minerals toward sulfide, Am J Sci, 292,659–
849 683, https://doi.org/10.2475/ajs.292.9.659, 1992.
850 Carstensen, J., Andersen, J.H., Gustafsson, B.G., Conley, D.J.: Deoxygenation of the Baltic Sea during the last century, Proc.
851 Natl. Acad. Sci. U.S.A., 111, 5628-5633, https://doi.org/10.1073/pnas.1323156111, 2014.
852 Chanton, J., Martens, C., and Goldhaber, M.: Biogeochemical cycling in an organic-rich coastal marine basin. 7. Sulfur mass
853 balance, oxygen uptake and sulfide retention: Geochimica et Cosmochimica Acta, 51, 1187-1199, 1987.
854 Chatterjee, S., Dickens, G.R., Bhatnagar, G., Chapman, W.G., Dugan, B., Snyder, G.T., Hirasaki, G.J.: Pore water sulfate,
855 alkalinity, and carbon isotope profiles in shallow sediment above marine gas hydrate systems: a numerical modeling
856 perspective, J. Geophys. Res. Solid Earth, 116, B09103, https://doi.org/ 10.1029/2011JB008290, 2011.
857 Chen, C.-T.A.: Shelf-vs. dissolution-generated alkalinity above the chemical lysocline, Deep-Sea Res. Part II, 49, 5365–
858 5375, https://doi.org/10.1016/S0967-0645(02)00196-0, 2002.
859 Chen, Y., Xu, S., Liu, W., Zhang, Z., Yang, T., Xiao, X., Deng, X., Li, J., Yao, H., Wu, Z.: Assessing biogeochemical
860 controls on porewater dissolved inorganic carbon cycling in the gas hydrate-bearing sediments of the Makran accretionary
861 wedge, Northeastern Arabian Sea off Pakistan, Front. Mar. Sci., 10, 1181921, https://doi.org/10.3389/fmars.2023.1181921,
862 2024.
863 Cline, J.D.: Spectrophotometric determination of hydrogen sulfide in natural waters, Limnol Oceanogr, 14, 454–458,
864 https://doi.org/10.4319/lo.1969.14.3.0454, 1969.

Coplen, T.B.: Guidelines and recommended terms for expression of stable-isotope-ratio and gas-ratio measurement results. Rapid Commun. Mass Spectrom., 25, 2538–2560, https://doi.org/10.1002/rcm.5129, 2011.

D'Hondt, S., Jørgensen, B.B., Miller, D.J., Batzke, A., Blake, R., Cragg, B.A., Cypionka, H., Dickens, G.R., et al.: Distributions of microbial activities in deep subseafloor sediments, Science, 306, 2216–2221, https://doi.org/10.1126/science.1101155, 2004.

De Grave, E., Vanderbruwaene, J., Van Bockstael, M.:^{57}Fe Mössbauer spectroscopic analysis of chlorite. Physics and Chemistry of Minerals 15, 173–180, https://doi.org/10.1007/BF00308781, 1987.

Dickens, A.F., Baldock, J.A., Smernik, R.J., Wakeham, S.G., Arnarson, T.S., Gélinas, Y., Hedges, J.I.: Solid-state ^{13}C NMR analysis of size and density fractions of marine sediments: Insight into organic carbon sources and preservation mechanisms, Geochim. Cosmochim. Acta, 70, 666– 686, https://doi.org/10.1016/j.gca.2005.10.024, 2006.

Dyar, M.D., Agresti, D.G., Schaefer, M.W., Grant, C.A., Sklute, E.C.: Mössbauer spectroscopy of Earth and planetary materials. Ann. Rev. Earth Planet. Sci., 34, 83–125, https://doi.org/10.1146/annurev.earth.34.031405.125049, 2006.

Egger, M., Rasigraf, O., Sapart, C.J., Jilbert, T., Jetten, M.S., Röckmann, T., van der Veen, C., Bândă, N., Kartal, B., Ettwig, K.F., Slomp, C.P.: Iron-mediated anaerobic oxidation of methane in brackish coastal sediments, Environ Sci Technol, 49, 277-83, https://doi.org/ 10.1021/es503663z, 2015.

Egger, M., Riedinger, N., Mogollón, J.M., Jørgensen, B.B.: Global diffusive fluxes of methane in marine sediments, Nat. Geosci., 11, 421–425, https://doi.org/10.1038/s41561-018-0122-8, 2018.

Ehlert von Ahn, C.M., Dellwig, O., Szymczycha, B., Kotwicki, L., Rooze, J., Endler, R., Escher, P., Schmiedinger, I., Sültenfuß, J., Diak, M., Gehre, M., Struck, U., Vogler, S., Böttcher, M.E.: Submarine groundwater discharge into a semi-enclosed coastal bay of the southern Baltic Sea: A multi-method approach. Oceanologia, 66, 111-138, https://doi.org/10.1016/j.oceano.2024.01.001, 2024.

Emerson, S., Hedges, J.: Chemical oceanography and the Marine Carbon Cycle. Cambridge University Press; 1st edition, 470 p., 2008.

Falkowska, L., Piekarek-Jankowska, H.: Submarine seepage of fresh groundwater: disturbance in hydrological and chemical structure of the water column in the Gdańsk Basin, Journal of Marine Science, 56, 153-160, https://doi.org/10.1006/JMSC.1999.0616, 1999.

Fennel, K., Testa, J.M.: Biogeochemical controls on coastal hypoxia, Annu. Rev. Mar. Sci., 11, 105-130, 10.1146/annurev-marine-010318-095138, 2019.

Friedlingstein, P., O'Sullivan, M., Jones, M. W., Andrew, R. M., Hauck, J., Olsen, A., et al.: Global carbon budget 2020, Earth Syst. Sci. Data, 12, 3269–3340, https://doi.org/10.5194/essd-12-3269-2020, 2020.

Froelich, P., Klinkhammer, G., Bender, M., Luedtke, N., Heath, G. R., Cullen, D., et al.: Early oxidation of organic matter in pelagic sediments of the eastern equatorial Atlantic: suboxic diagenesis, Cosmochim. Cosmochim. Acta, 43, 1075–1090, https://doi.org/10.1016/0016-7037(79)90095-4, 1979.

Grasshoff, K., Kremling, K., Ehrhardt, M.: Methods of Seawater Analysis 3rd Ed., Wiley-VCH, Weinheim, 1999.

Glud, R.N.: Oxygen dynamics of marine sediments, Mar. Biol. Res., 4, 243–289, https://doi.org/10.1080/17451000801888726, 2008.

Gregg, J.M., Bish, D.L., Kaczmarek, S.E., Machel, H.G.: Mineralogy, nucleation and growth of dolomite in the laboratory and sedimentary environment: A review, Sedimentology, 62, 1749–1769, https://doi.org/10.1111/sed.12202, 2015.

Griffiths, J.R., Kadin, M., Nascimento, F.J.A., Tamelander, T., Törnroos, A., Bonaglia, S., et al.: The importance of benthic-pelagic coupling for marine ecosystem functioning in a changing world, Glob. Chang. Biol., 23, 2179–2196, https://doi.org/10.1111/gcb.13642, 2017.

Gustafsson E., Hagens M., Sun X., Reed D.C., Humborg C., Slomp C.P., Gustafsson B.G.: Sedimentary alkalinity generation and long-term alkalinity development in the Baltic Sea, Biogeosciences, 16, 437–456, https://doi.org/10.5194/bg-16-437-2019, 2019.

Han, L.-F., Niel Plummer, L., Aggarwal, P.: The curved 14 C vs. δ 13 C relationship in dissolved inorganic carbon: A useful tool for groundwater age- and geochemical interpretations. Chemical Geology, 387, 111–125, https://doi.org/10.1016/j.chemgeo.2014.08.026, 2014.

Hedges, J.I., Keil, R.G.: Sedimentary organic-matter preservation—an assessment and speculative synthesis. Mar. Chem. 49, 81–115, 1995.

Hedges, J.I., Keil, R.G.; Benner, R.: What happens to terrestrial organic matter in the ocean?, Org. Geochem., 27, 195– 212, https://doi.org/10.1016/S0146-6380(97)00066-1, 1997.

Hedges I., Stern J.: Carbon and nitrogen determinations of carbonate containing solids. Limnol. Oceanogr., 29, 657–663, 1984.

Iversen, N., Jørgensen, B.B.: Anaerobic methane oxidation rates at the sulfate-methane transition in marine sediments from Kattegat and Skagerrak (Denmark), Limnol. Oceanogr., 30, 944–955, https://doi.org/10.4319/lo.1985.30.5.0944, 1985.

Jilbert, T., Cowie, G., Lintumäki, L., Jokinen, S., Asmala, E., Sun, X., Mörth, C-M., Norkko, A., Humborg, C.: Anthropogenic Inputs of Terrestrial Organic Matter Influence Carbon Loading and Methanogenesis in Coastal Baltic Sea Sediments, Front. Earth Sci., 9, 716416, https://doi.org/10.3389/feart.2021.716416, 2021.

Jørgensen, B.B., Bang, M., Blackburn, T.H.: Anaerobic mineralization in marine-sediments from the Baltic-Sea-North-Sea transition, Mar. Ecol. Prog. Ser., 59, 39–54, http://www.jstor.org/stable/24842420, 1990.

Jørgensen N.O.: Methane-derived carbonate cementation of marine sediments from the Kattegat, Denmark: geochemical and geological evidence, Mar. Geol., 103, 1–13, https://doi.org/10.1016/0025-3227(92)90006-4, 1992.

Jørgensen, B.B., Weber, A., Zopfi, J.: Sulfate reduction and anaerobic oxidation in Black Sea sediments, Deep-Sea Res. Part I, 48, 2097–2120, https://doi.org/10.1016/S0967-0637(01)00007-3, 2001.

Jørgensen, B.B., Kasten, S.: Sulfur cycling and methane oxidation, in Marine geochemistry edited by: Schulz, H.D., Zabel, M., Berlin, Heidelberg: Springer, 2006.

Jönsson A., Danielsson Å., Rahm L.: Bottom type distribution based on wave friction velocity in the Baltic Sea. Cont. Shelf Res., 25, 419–435, https://doi.org/10.1016/j.csr.2004.09.011, 2005.

Ketzer, M., Stranne, C., Rahmati-Abkenar, M., Shahabi-Ghahfarokhi, S., Jaeger, L., Pivel, M.A.G., Josefsson, S., Zillén, L.:, Near seafloor methane flux in the world's largest human-induced dead zone is regulated by sediment accumulation rate, Marine Geology, 468, 107220, https://doi.org/10.1016/j.margeo.2024.107220, 2024.

Kowalski, W., Mazurek, Z., Mazurek, A.: Geochemiczno mineralogiczna charakterystyka marmurów dolomitycznych ze złoża Rędziny (in Polish). Geol. Quart. 20, 21–34. 1976.

Kozerski, B., Macioszczyk, A., Pazdro, Z., Sadurski, A., 1987. Fluoride in groundwater of the Gdańsk region. Ann. Soc. Geol. Pol. 57, 349–374 (in Polish).

Krumins, V., Gehlen, M., Arndt, S., Van Cappellen, P., Regnier, P.: Dissolved inorganic carbon and alkalinity fluxes from coastalmarine sediments: model estimates for different shelf environments and sensitivity to global change, Biogeosciences, 10, 371–398, https://doi.org/10.5194/bg-10-371-2013, 2013.

Liu, Kk, Atkinson, L., Quinones, R., Talaue-McManus, L.: Carbon and Nutrient Fluxes in Continental Margins: A Global Synthesis, Springer-Verlag Berlin Heidelberg, https://doi.org/10.1007/978-3-540-92735-8, 2010.

Liu, D., Fan, Q., Papineau, D., Yu, N., Chu, Y., Wang, H., Qiu, X., Wang, X.: Precipitation of protodolomite facilitated by sulfate-reducing bacteria: The role of capsule extracellular polymeric substances Chem. Geol., 533, 119415, https://doi.org/10.1016/j.chemgeo.2019.119415, 2020.

Lukoczki, G., Bish, D., Gregg, J.M.: A best-practices guide to X-ray diffraction studies of sedimentary carbonates. Sed. Geol. 493, 107028. https://doi.org/10.1016/j.sedgeo.2026.107028, 2026.

Łukawska-Matuszewska, K., Dwornik, M.: Early diagenesis in anoxic sediments of the Gulf of Gdańsk (southern Baltic Sea): Implications for porewater chemistry and benthic flux of carbonate alkalinity. Front. Earth Sci., 13, 1593031, https://doi.org/10.3389/feart.2025.1593031, 2025.

Łukawska-Matuszewska, K., Brodecka-Goluch, A., Czachor, A., Rios-Quintero, R.: Gas bubble release areas as new potential hot spots for water column enrichment with nutrients in eutrophicated sea, Mar. Env. Res., 205, 106981, https://doi.org/10.1016/j.marenvres.2025.106981, 2025.

Łukawska-Matuszewska, K., Graca, B., Brocławik, O., Zalewska T.: The impact of declining oxygen conditions on pyrite accumulation in shelf sediments (Baltic Sea), Biogeochemistry, 142, 209–230, https://doi.org/10.1007/s10533-018-0530-2, 2019.

Łukawska-Matuszewska K., Kiełczewska J.: Effects of near-bottom water oxygen concentration on biogeochemical cycling of C, N and S in sediments of the Gulf of Gdansk (southern Baltic), Continental Shelf Research, 117, 30-42, https://doi.org/10.1016/j.csr.2016.02.001, 2016.

Majewski, P., Klusek, Z.: Parametters of echo signals originated from a gas seepage site in the southern Baltic Sea, Hydroacoustics. 17, 143–150, 2014.

Maksymowska, D., Richard, P., Piekarek-Jankowska, H., Riera, P.: Chemical and isotopic composition of the organic matter sources in the Gulf of Gdansk (Southern Baltic Sea), Estuarine, Coastal and Shelf Science, 51, 585–598, https://doi.org/10.1006/ecss.2000.0701, 2000.

967 Malinverno, A., Pohlman J.W.: Modeling sulfate reduction in methane hydrate-bearing continental margin sediments: Does
968 a sulfate-methane transition require anaerobic oxidation of methane? Geochem. Geophys. Geosyst., 12, Q07006,
969 https://doi.org/10.1029/2011GC003501, 2011.
970 Maltby, J., Steinle, L., Löscher, C. R., Bange, H. W., Fischer, M. A., Schmidt, M., Treude, T.: Microbial methanogenesis in
971 the sulfate-reducing zone of sediments in the Eckernförde Bay, SW Baltic Sea, Biogeosciences, 15, 137–15,
972 https://doi.org/10.5194/bg-15-137-2018, 2018.
973 Masuzawa, T., Handa, N., Kitagawa, H., Kusakabe, M., 1992. Sulfate reduction using methane in sediments beneath a
974 bathyal cold seep giant clam community off Hatsushima-Island, Sagami Bay, Japan. Earth Planet. Sci. Lett., 110, 39-50,
975 https://doi.org/10.1016/0012-821X(92)90037-V,1992.
976 Matciak, M., Misiewicz, M.M., Szymczycha, B., Idczak, J., Tęgowski, J., Diak, M.: Pockmarks and associated fresh
977 submarine groundwater discharge in the seafloor of Puck Bay, southern Baltic Sea, Science of The Total Environment, 942,
978 173617, https://doi.org/10.1016/j.scitotenv.2024.173617, 2024.
979 Meister, P., Liu, B., Khalili, A., Böttcher, M.E., Jørgensen, B.B.: Factors controlling the carbon isotope composition of
980 dissolved inorganic carbon and methane in marine porewater: an evaluation by reaction-transport modelling, J. Mar. Syst.,
981 200, 103227, https://doi.org/10.1016/j.jmarsys.2019.103227, 2019.
982 Meyers, P.A.: Preservation of elemental and isotopic source identification of sedimentary organic matter, Chem. Geol., 114,
983 289–302, https://doi.org/10.1016/0009-2541(94)90059-0, 1994.
984 Meyers, P.A.: Organic geochemical proxies of paleoceanographic, paleolimnologic, and paleoclimatic processes, Organic
985 Geochemistry, 27, 213–250, https://doi.org/10.1016/S0146-6380(97)00049-1, 1997.
986 Miller, C.M., Dickens, G.R., Jakobsson, M., Johansson, C., Koshurnikov, A., O'Regan, M., Muschitiello, F., Stranne, C.,
987 Mörth, C.-M.: Pore water geochemistry along continental slopes north of the East Siberian Sea: inference of low methane
988 concentrations, Biogeosciences, 14, 2929–2953, https://doi.org/10.5194/bg-14-2929-2017, 2017.
989 Miltner A., Emeis K-C.: Terrestrial organic matter in surface sediments of the Baltic Sea, Northwest Europe, as determined
990 by CuO oxidation, Geochim. Cosmochim. Acta, 65, 1285–1299, https://doi.org/10.1016/S0016-7037(00)00603-7, 2001.
991 Moore, D.M., Reynolds, R.C.Jr.: X-Ray Diffraction and the Identification and Analysis of Clay Minerals (2nd Ed.). Oxford
992 University Press, Oxford, 379 pp., 1997.
993 Mucci, A., Sundby, B., Gehlen, M., Arakaki, T., Zhong, S., Silverberg, N.: The fate of carbon in continental shelf sediments
994 of eastern Canada: a case study, Deep-Sea Res. Pt. II., 47, 733-760, https://doi.org/10.1016/S0967-0645(99)00124-1, 2000.
995 Myllykangas, JP., Hietanen, S., Jilbert, T.: Legacy Effects of Eutrophication on Modern Methane Dynamics in a Boreal
996 Estuary, Estuaries and Coasts, 43, 189–206, https://doi.org/10.1007/s12237-019-00677-0, 2020.
997 Nöthen, K., Kasten, S.: Reconstructing changes in seep activity by means of pore water and solid phase Sr/Ca and Mg/Ca
998 ratios in pockmark sediments of the Northern Congo Fan, Mar. Geol., 287, 1–13,
999 https://doi.org/10.1016/j.margeo.2011.06.008, 2011.

Paerl, H.W., Hall, N.S., Peierls, B.L., Rossignol, K.L.: Evolving paradigms and challenges in estuarine and coastal eutrophication dynamics in a culturally and climatically stressed world, Estuar. Coasts, 37, 243–258, http://www.jstor.org/stable/44851148, 2014.

Parkhust, D.L., Appelo, C.A.J.: Description of Input and Examples for PHREEQC Version 3—A Computer Program for Speciation, Batch-Reaction, One-Dimensional Transport, and Inverse Geochemical Calculations. US Geological Survey Techniques and Methods, Book 6, Chapter A43, 497 p. http://pubs.usgs.gov/tm/06/a43, 2013.

Piekarek-Jankowska, H., Matciak, M., Nowacki, J.: Salinity variations as an effect of groundwater seepage through the seabed (Puck Bay. Poland), Oceanologia, 36,1, 33-46, 1994.

Piker, L., Schmaljohann, R., Imhoff, J.F.: Dissimilatory sulfate reduction and methane production in Gotland Deep sediments (Baltic Sea) during a transition period from oxic to anoxic bottom water (1993-1996), Aquat. Microb. Ecol., 14, 183–193, https://doi.org/10.3354/ame014183, 1998.

Pimenov, N.V., Ul'yanova, M.O., Kanapatskii, T.A., Sivkov V.V., Ivanov, M.V.: Microbiological and biogeochemical processes in a pockmark of the Gdansk depression, Baltic Sea, Microbiology **77**, 579–586, https://doi.org/10.1134/S0026261708050111, 2008.

Pimenov, N.V., Ulyanova, M.O., Kanapatsky, T.A., Veslopolova, E.F., Sigalevich, P.A., Sivkov, V.V.: Microbially mediated methane and sulfur cycling in pockmark sediments of the Gdansk Basin, Baltic Sea. Geo-Mar Lett., 30, 439–448, https://doi.org/10.1007/s00367-010-0200-4, 2010.

Pimenov, N.V., Ul'yanova, M.O., Kanapatskii, T.A., Mitskevich, I.N., Rusanov, I I., Sigalevich, P.A., et al.: Sulfate reduction, methanogenesis, and methane oxidation in the upper sediments of the Vistula and Curonian Lagoons, Baltic Sea, Microbiology 82, 224–233, https://doi.org/10.1134/S0026261713020136, 2013.

Rabalais, N.N., Diaz, R.J., Levin, L.A., Turner, R.E., Gilbert, D., Zhang, J.: Dynamics and distribution of natural and human-caused hypoxia, Biogeosciences, 7, 585-619, https://doi.org/10.5194/bg-7-585-2010, 2010.

Raiswell, R., Berner, R.A.: Pyrite formation in euxinic and semi-euxinic sediments, Am J Sci, 285, 710–724, https://doi.org/10.2475/ajs.285.8.710, 1985.

Rassmann, J., Lansard, B., Pozzato, L., Rabouille, C.H.: Carbonate chemistry in sediment pore waters of the Rhône River delta driven by early diagenesis (NW Mediterranean), Biogeosciences, 13, 5379–5394, https://doi.org/10.5194/bg-13-5379-2016, 2016.

Reeburg, W.S.: Oceanic methane biogeochemistry, Chem. Rev., 107, 486–513, https://doi.org/10.1021/cr050362v, 2007.

Rothwell, K.A., ThomasArrigo, L.K., Kaegi, R., Kretzschmar, R.: Low molecular weight organic acids stabilise siderite against oxidation and influence the composition of iron (oxyhydr)oxide oxidation products, Environmental Science: Processes & Impacts 27, 133–145, https://doi.org/10.1039/D4EM00363B, 2025.

Rzepa G., Borkowski A., Manecki M., Brodecka-Goluch A., Łukawska-Matuszewska K., Kania J., Błachowski A., Działak P., De Mey-Śnieżyńska I.: The effect of freshwater discharge on the microbial-induced precipitation of minerals in a Baltic Sea bottom pockmark, Oceanologia, https://doi.org/10.5697/NDCH3019, in press.

Sawicka, J.E., Brüchert, V.: Annual variability and regulation of methane and sulfate fluxes in Baltic Sea estuarine sediments, Biogeosciences, 14, 325–339, https://doi.org/10.5194/bg-14-325-2017, 2017.

Sadurski, A.: Warunki hydrochemiczne utworów kredowych w rejonie Gdańska, Geological Quarterly 29, 405-418 (in Polish), 1985.

Schlünz, B., Schneider, R.R.: Transport of Terrestrial Organic Carbon to the Oceans by Rivers: Re-estimating Flux- and Burial Rates, Int. J. Earth Sci., 88, 599–606, https://doi.org/10.1007/s005310050290, 2020.

Soetaert, K., Herman, P. M.J., Middelburg, J.J.: A model of early diagenetic processes from the shelf to abyssal depths, Geochim. Cosmochim. Acta, 60, 1019–1040, https://doi.org/10.1016/0016-7037(96)00013-0, 1996.

Struck, U., Emeis, K., Voss, M., Christiansen, C., Kunzendorf, H.: Records of southern and central Baltic Sea eutrophication in $\delta^{13}C$ and $\delta^{15}N$ of sedimentary organic matter. Mar. Geol., 164, 157-171, 2000.

Sun, J., Wu, Z., Cheng, H., Zhang, Z., Frost, R.L.: A Raman spectroscopic comparison of calcite and dolomite. Spectrochim Acta A, 117, 158–162, https://doi.org/10.1016/j.saa.2013.08.014, 2014.

Szymczycha, B., Vogler, S., Pempkowiak, J.: Nutrient fluxes via submarine groundwater discharge to the Bay of Puck, southern Baltic Sea, Science of The Total Environment, 438, 86–93, https://doi.org/10.1016/j.scitotenv.2012.08.058, 2012.

Szymczycha, B., Miotk, M., Pempkowiak, J.: Submarine groundwater discharge as a source of mercury in the Bay of Puck, the Southern Baltic Sea, Water Air Soil Pollut, 224, https://doi.org/10.1007/s11270–013-1542-0, 2013.

Szymczycha, B., Böttcher, M.E., Diak, M., Koziorowska-Makuch, K., Kuliński, K., Makuch, P., Ehlert von Ahn C.M., Winogradow, A.: The benthic-pelagic coupling affects the surface water carbonate system above groundwater-charged coastal sediments, Front. Mar. Sci., 10, 1218245, https://doi.org/10.3389/fmars.2023.1218245, 2023.

Thamdrup, B., Canfield, D.E.: Pathways of carbon oxidation in continental margin sediments off central Chile, Limnol. Oceanogr., 41, 1629–1650, https://doi.org/10.4319/lo.1996.41.8.1629, 1996.

Thang, N.M., Brüchert, V., Formolo, M., Wegener, G., Ginters, L., Jørgensen, B.B.: The Impact of Sediment and Carbon Fluxes on the Biogeochemistry of Methane and Sulfur in Littoral Baltic Sea Sediments (Himmerfjärden, Sweden), Estuaries and Coasts, 36, 98–115, https://doi.org/10.1007/s12237-012-9557-0, 2013.

Thomas, H., Schiettecatte, L.-S., Suykens, K., Koné, Y.J.M., Shadwick, E.H., Prowe, A.E.F., Bozec, Y., de Baar, H.J.W., Borges, A.V.: Enhanced ocean carbon storage from anaerobic alkalinity generation in coastal sediments, Biogeosciences, 6, 267–274, https://doi.org/10.5194/bg-6-267-2009, 2009.

Thomsen, T.R., Finster, K., Ramsing, N.B.: Biogeochemical and molecular singatures of anaerobic methane oxidation in marine sediment, Appl. Environ. Microbiol., 67, 1646-1656, https://doi.org/10.1128/AEM.67.4.1646-1656.2001, 2001.

Treude, T., Krüger, M., Boetius, A., Jørgensen, B.B.: Environmental control on anaerobic oxidation of methane in the gassy sediments of Eckernförde Bay (German Baltic), Limnol. Oceanogr., 50, 1771–1786, https://doi.org/10.4319/lo.2005.50.6.1771, 2005.

Treude, T., Orphan, V., Knittel, K., Gieseke, A., House, C.H., Boetius, A.: Consumption of Methane and CO2 by Methanotrophic Microbial Mats from Gas Seeps of the Anoxic Black Sea, Applied and Environmental Microbiology, 73, 2271–2283, https://doi.org/10.1128/AEM.02685-06, 2007.

Tyrrell, T., Schneider, B., Charalampopoulou, A., Riebesell, U.: Coccolithophores and calcite saturation state in the Baltic and Black Seas, Biogeosciences, 5, 485–494, https://doi.org/10.5194/bg-5-485-2008, 2008.

Uścinowicz Sz.: Geochemistry of Baltic Sea surface sediments. Polish Geolog. Inst.-National Res. Inst., Warsaw, 356 p., 2011.

Wada, E., Hattori, A.: Nitrogen in the Sea: Forms, Abundances, and Rate Processes. CRC Press, Boca Raton, 208 pp., 1991.

Walter, L.M., Ku, T.C. W., Muehlenbachs, K., Patterson, W. P., Bonnell, L.: Controls on the δ13C of dissolved inorganic carbon in marine pore waters: An integrated case study of isotope exchange during syndepositional recrystallization of biogenic carbonate sediments (South Florida Platform, USA), Deep Sea Research Part II: Topical Studies in Oceanography, 54, 1163–1200, https://doi.org/10.1016/j.dsr2.2007.04.014, 2007.

Wang, C., Su, J., Song, L., Qiao, P., Fan, D.: Response of early diagenesis to methane leakage in the inner shelf of the East China Sea, Front. Mar. Sci., 11, 1410241, https://doi.org/10.3389/fmars.2024.1410241, 2024.

Whiticar, M.J.: Carbon and hydrogen isotope systematics of bacterial formation and oxidation of methane. Chem. Geol. 161, 291–314, https://doi.org/10.1016/10.1016/S0009-2541(99)00092-3, 1999.

Wollast, R.: Evaluation and comparison of the global carbon cycle in the coastal zone and in the open ocean. In: Brink, K.H., Robinson, A.R. (Eds.), The Sea. John Wiley, New York, pp. 213–252, 1998.

Xu C., Wu N., Sun Z., Zhang X., Geng W., Cao H., et al.: Methane seepage inferred from pore water geochemistry in shallow sediments in the western slope of the Mid-Okinawa Trough, Mar. Pet. Geol., 98, 306–315, https://doi.org/10.1016/j.marpetgeo.2018.08.021, 2018.

Yadav, V.B., Pulhani, V.A., Kumar, A.V.: Study of sedimentary organic carbon using δC, δN and TOC/TN as indicator in sediment core samples from Mumbai Harbor Bay, Environmental Monitoring and Assessment, 197, 552, 10.1007/s10661-025-13980-0, https://doi.org/10.1007/s10661-025-13980-0, 2025.

Zalewska, T., Przygrodzki, P., Suplińska, M., Saniewski, M.: Geochronology of the southern Baltic Sea sediments derived from 210Pb dating, Quaternary Geochronology, 56, 101039, https://doi.org/10.1016/j.quageo.2019.101039, 2020.

Zha, R., Yang, T., Shi, X., Su, P., Fang, Y.: Quantitative assessment of dissolved inorganic carbon cycling in marine sediments from gas hydrate-bearing areas in the South China Sea, Mar. Petrol. Geol., 145, 105881, https://doi.org/10.1016/j.marpetgeo.2022, 2022.

Zheng, W., Liu, D., Yang, S., Fan, Q., Papineau, D., Wang, H., Qiu, X., Chang, B., She, Z.: Transformation of protodolomite to dolomite proceeds under dry-heating conditions. Earth Planet. Sci. Lett., 576, 117249, https://doi.org/10.1016/j.epsl.2021.117249, 2021.